

ROUTE, INTERPRET, REPEAT: BLURRING THE LINE BETWEEN POST HOC EXPLAIN- ABILITY AND INTERPRETABLE MODELS

Shantanu Ghosh

Department of Electrical and Computer Engineering
Boston University
Boston, MA 02215, USA
shawn24@bu.edu

Ke Yu

Intelligent Systems Program
University of Pittsburgh
5607 Baum Blvd, Pittsburgh, PA 15206
yu.ke@pitt.edu

Forough Arabshahi

Meta AI
1 Hacker Way Menlo Park, CA 94025
forough@meta.com

Kayhan Batmanghelich

Department of Electrical and Computer Engineering
Boston University
Boston, MA 02215, USA
kayhan@bu.edu

ABSTRACT

The current approach to ML model design is either to choose a flexible Blackbox model and explain it post hoc or to start with an interpretable model. Blackbox models are flexible but difficult to explain, whereas interpretable models are designed to be explainable. However, developing interpretable models necessitates extensive ML knowledge, and the resulting models tend to be less flexible, offering potentially subpar performance compared to their Blackbox equivalents. This paper aims to blur the distinction between a post hoc explanation of a BlackBox and constructing interpretable models. We propose beginning with a flexible BlackBox model and gradually *carving out* a mixture of interpretable models and a *residual network*. Our design identifies a subset of samples and *routes* them through the interpretable models. The remaining samples are routed through a flexible residual network. We adopt First Order Logic (FOL) as the interpretable model’s backbone, which provides basic reasoning on concepts retrieved from the BlackBox model. On the residual network, we repeat the method until the proportion of data explained by the residual network falls below a desired threshold. Our approach offers several advantages. First, the mixture of interpretable and flexible residual networks results in almost no compromise in performance. Second, the route, interpret, and repeat approach yields a highly flexible interpretable model. Our extensive experiment demonstrates the performance of the model on various datasets. We show that by editing the FOL model, we can fix the shortcut learned by the original BlackBox model. Finally, our method provides a framework for a hybrid symbolic-connectionist network that is simple to train and adaptable to many applications.

1 INTRODUCTION

Model explainability is essential in high-stakes applications of AI, such as healthcare. While BlackBox models (*e.g.*, Deep Learning) offer flexibility and modular design, post hoc explanation is prone to confirmation bias Wan et al. (2022), lack of fidelity to the original model Adebayo

et al. (2018), and insufficient mechanistic explanation of the decision-making process Rudin (2019). Interpretable-by-design models do not suffer from those issues but tend to be less flexible than Blackbox models and demand substantial expertise to design and fine-tune. Using post hoc explanation or adopting an interpretable model is a mutually exclusive decision to be made at the initial phase of AI model design. This paper aims to blur the line on that dichotomous model design.

The literature on post hoc explainable AI is extensive. The methods such as model attribution (e.g., Saliency Map Simonyan et al. (2013); Selvaraju et al. (2017)), counterfactual approach Abid et al. (2021); Singla et al. (2019), and distillation methods Alharbi et al. (2021); Cheng et al. (2020) are examples of post hoc explainability approaches. Those methods either identify important features of input that contribute the most to the network’s output Shrikumar et al. (2016), generate perturbation to the input that flips the network’s output Samek et al. (2016), Montavon et al. (2018), or estimate simpler functions that locally approximate the network output. The advantage of the post hoc explainability methods is that they do not compromise the flexibility and performance of the BlackBox. However, the post hoc explainability method suffers from several undesirable significant drawbacks, such as a lack of fidelity and mechanistic explanation of the network output Rudin (2019). Without a mechanistic explanation, recourse to a model’s undesirable behavior is unclear. Interpretable models are alternative designs to the BlackBox model that do not suffer from many of those drawbacks.

Interpretable models also have a long history in statistics and machine learning Letham et al. (2015); Breiman et al. (1984). Several families of interpretable models exist, such as the rule-based approach and generalized additive models Hastie & Tibshirani (1987). Many methods focus on tabular or categorical data and less on high-dimensional structured data such as images. Interpretable models for structured data rely mostly on projecting to a lower dimensional *concept* or *symbolic* space that is understandable for humans Koh et al. (2020). Aside from a few exceptions Ciravegna et al. (2021); Barbiero et al. (2022), the current State-Of-The-Art (SOTA) design does not model the interaction between concepts and symbols, hence offering limited reasoning capabilities and less robustness. Furthermore, current designs are not as flexible as the Blackbox model, which may compromise the performance of such models.

We aim to achieve the best of both worlds: the flexibility of the BlackBox and the mechanistic explainability of the interpretable models. The general idea is that a single interpretable model may not be sufficiently powerful to explain all samples, and several interpretable models might be hidden inside the Blackbox model. We construct a hybrid neuro-symbolic model by progressively *carving out* a mixture of interpretable model and a *residual network*. Our design identifies a subset of samples and *routes* them through the interpretable models. The remaining samples are routed through a flexible residual network. We adopt First Order Logic (FOL) as the interpretable model’s backbone, which provides basic reasoning on concepts retrieved from the BlackBox model. On the residual network, we repeat the method until the proportion of data explained by the residual network falls below a desired threshold. The experimental results across various computer vision and medical imaging datasets reveal that our method accounts for the diversity of the explanation space and has minimal impact on the Blackbox’s performance. Additionally, we apply our method’s explanations to detect shortcuts in computer vision and successfully eliminate the bias from the Blackbox’s representation.

2 RELATED WORK

Post hoc explanations Simonyan et al. (2013); Selvaraju et al. (2017); Smilkov et al. (2017) discuss the post hoc based explanation method using saliency maps to explain a convolution neural network. This method aims to highlight the pixels in the input images that contributed to the network’s prediction. Adebayo et al. (2018); Kindermans et al. (2019) demonstrates that the saliency maps highlight the correct regions in the image even though the backbone’s representation was arbitrarily perturbed. Additionally, in LIME Ribeiro et al. (2016), given a superpixel, a surrogate linear function attempts to learn the prediction of the Blackbox surrounding that superpixel. SHAP Lundberg & Lee (2017) utilizes a prominent game-theoretic strategy called SHAPLY values to estimate the Blackbox’s prediction by considering all the permutations of adding and removing a specific feature to determine its importance in the final prediction. Having the explanations in terms of pixel intensities, they do not correspond to the high-level interpretable attributes (*concept*), understood by

humans. In this paper, we aim to provide the post hoc explanation of the Blackbox in terms of the interpretable concepts, rather than the pixel intensities.

Interpretable models In this class, the researchers try to design inherently interpretable models to eliminate the requirement for post hoc explanations. In the literature, we find interpretable models in Generalized Additive Models (GAM) Hastie & Tibshirani (1987), or on logic formulas, as in Decision Trees Breiman et al. (1984) or Bayesian Rule Lists (BRL) Letham et al. (2015). However, most of these methods work well in categorical datasets rather than continuous data such as images. Additionally, Chen et al. (2019) introduces a “case-based reasoning” technique, known as “ProtoP-Net”. Here, the authors first dissect an image in Prototypical parts and then classifies by combining evidence from the pre-defined prototypes. This method is highly sensitive to the choice of prototypes and the distance metric used to compare with the prototype. So instead of using any prototypes, our proposed method uses human understandable concepts to build the mixture of interpretable models.

Concept-based interpretable models Recently, Concept bottleneck models (CBM) Koh et al. (2020) leverage the weak annotations of visual attributes as high-level human-comprehensible concepts Kim et al. (2017) in a fine-grained image classification dataset to predict the concepts from input images. Subsequently, the downstream classifier predicts the class labels from the discovered concepts. However, they do not explain how the final classifier composes those concepts for prediction. E-Lens Barbiero et al. (2022) addresses this gap by introducing an entropy-based classifier into the CBM pipeline to predict the class labels from the concepts and provide explanations in terms of first-order logic (FOL) using the concepts. Later, Yuksekgonul et al. (2022) introduces the Post hoc-concept-based model (PCBM) to learn the concepts from the backbone of a trained Blackbox and utilize an interpretable classifier to learn the class labels from the concepts. In addition, they propose the Hybrid-Post hoc-concept-based model (PCBM-h) to replicate the performance of the original Blackbox by fitting the unexplained portion of the Blackbox. However, all these methods employ a single interpretable model to explain a Blackbox, failing to apprehend different form of explanations for different samples. This paper proposes that a single interpretable model may not be sufficient to capture the diversity of explanations for all samples used by the Blackbox. We address this issue by introducing a mixture of interpretable models that utilizes the Blackbox’s flexibility and offer a local explanation.

3 METHOD

Notation Assume we have a dataset $\{\mathcal{X}, \mathcal{Y}, \mathcal{C}\}$, where \mathcal{X} , \mathcal{Y} , and \mathcal{C} are the input images, class labels, and human interpretable attributes, respectively. $f^0 : \mathcal{X} \rightarrow \mathcal{Y}$, is a pre-trained deep neural network (our initial Blackbox model), trained only with supervision from the labels \mathcal{Y} . We assume that f^0 is a composition $h^0 \circ \Phi$, where $\Phi : \mathcal{X} \rightarrow \mathbb{R}^l$ is the image embeddings and $h^0 : \mathbb{R}^l \rightarrow \mathcal{Y}$ is a transformation from the embeddings, Φ , to the class labels. We denote the learnable function $t : \mathbb{R}^l \rightarrow \mathcal{C}$, projecting the image embeddings to the concept space. The concept space is the space spanned by the attributes \mathcal{C} . Per this definition, function t outputs a scalar value representing a concept for each input image.

Method Overview Figure 1 shows an overview of our approach. We aim to iteratively carve out an interpretable model from the given Blackbox model. Each iteration results in an interpretable model (the downward grey paths in Figure 1) and a residual (the straightforward black paths in Figure 1). We start this process with f^0 – the initial Blackbox given to us. At iteration k , we distill the Blackbox of the previous iteration f^{k-1} with a neuro-symbolic interpretable model, $g^k : \mathcal{C} \rightarrow \mathcal{Y}$. We generate explanations in terms of First Order Logic (FOL) from g^k as suggested by Barbiero et al. (2022). We coin the term *residual* r^k to refer to the portion of f^{k-1} that g^k cannot explain, specifically $r^k = f^{k-1} - g^k$. We then approximate r^k with $f^k = h^k(\phi(.))$. f^k will be the Blackbox for the subsequent iterations and be explained by the respective interpretable models. A learnable gating mechanism, denoted by $\pi^k : \mathcal{C} \rightarrow \{0, 1\}$ (shown as the selector in figure 1) is responsible for routing an input image towards either g^k or r^k . The thickness of the lines in Figure 1 represents the samples covered by the interpretable models (grey line) and the residuals (black line). With every iteration, the cumulative coverage of the interpretable models increases, but the residual decreases. We name our method *route*, *interpret* and *repeat*.

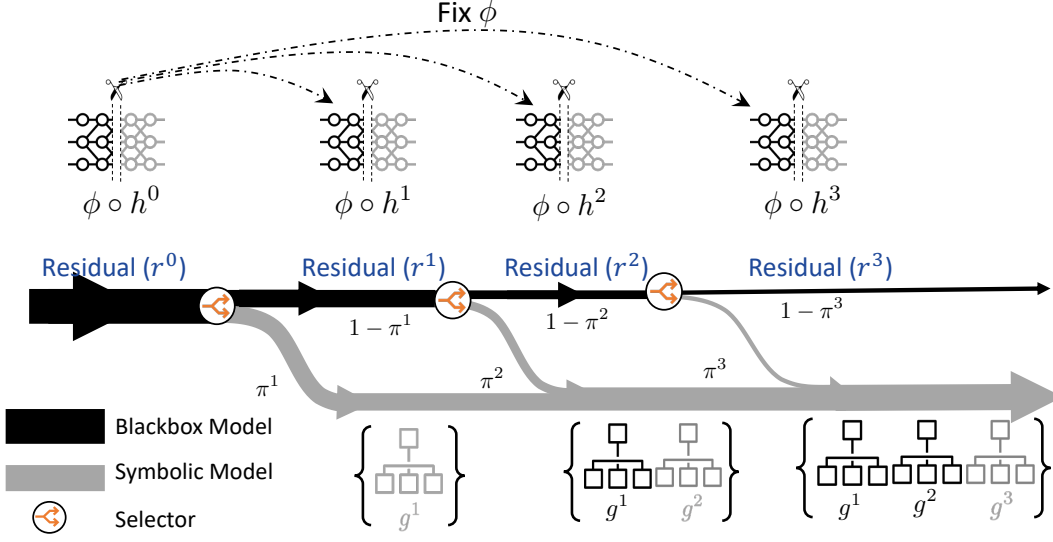


Figure 1: Schematic view of *route*, *interpret* and *repeat*. At step k , the selector *routes* each sample either towards the interpretable model g^k (to *interpret*) with probability π^k or the residual (to *repeat* in the further iterations) $r^k = f^{k-1} - g^k$ with probability $1 - \pi^k$. Here, f^{k-1} is the Blackbox of the previous iteration, $k - 1$. If the sample goes through g^k , we obtain the explanations for that sample in terms of First Order Logic (FOL). Otherwise, the sample goes through the next step until it either goes through a subsequent interpretable model or reaches the last residual. Note that components in black and grey indicate the fixed and trainable modules in our model.

3.1 NEURO-SYMBOLIC KNOWLEDGE DISTILLATION

Knowledge distillation in our method involves three parts. (1) a series of trainable soft attention scores that *routes* each sample through the interpretable models and the residual networks, (2) A sequence of learnable neuro-symbolic interpretable models, each providing FOL explanations to *interpret* the Blackbox, and (3) *repeating* with Residual networks for the samples that cannot be explained with their interpretable counterparts. We explain each component in detail in what follows.

3.1.1 THE SELECTOR FUNCTION

The first step of our method is to *route* an input sample through the interpretable model g^k and residuals r^k using a series of soft attention scores π^k for $k \in [0, K]$, where K is the number of iterations. We denote this as the selector in figure 1. Specifically, at each iteration k , the specific selector *routes* a sample $\{x_j, y_j, c_j\}$ towards g^k and r^k with probability $\pi^k(c_j)$ and $1 - \pi^k(c_j)$

respectively. We define the empirical coverage of the k^{th} iteration as, $\zeta(\pi^k) = \frac{1}{m} \sum_{j=1}^m \pi^k(c_j)$, the

empirical mean of the samples selected by the selector for the corresponding interpretable model g^k , with m being the total number of samples in the training set. Thus the total selective risk is,

$$\mathcal{R}^k(\pi^k, g^k) = \frac{\frac{1}{m} \sum_{j=1}^m \mathcal{L}_{(g^k, \pi^k)}^k(x_j, c_j)}{\zeta(\pi^k)}, \quad (1)$$

where $\mathcal{L}_{(g^k, \pi^k)}^k$ is the optimization loss used to learn g^k and π^k together, discussed in section 3.1.2. For a given coverage of $\tau^k \in (0, 1]$, we solve the following optimization problem

$$\theta_{s^k}^*, \theta_{g^k}^* = \min_{\theta_{s^k}, \theta_{g^k}} \mathcal{R}^k(\pi^k(.; \theta_{s^k}), g^k(.; \theta_{g^k})) \quad \text{s.t.} \quad \zeta(\pi^k(.; \theta_{s^k})) \geq \tau^k \quad (2)$$

For k^{th} iteration, $\theta_{s^k}^*, \theta_{g^k}^*$ are the optimal parameters for the selector π^k and the interpretable model g^k respectively. In this work, π^k 's are neural networks with sigmoid activation. At inference time, the concept vector c_j of sample x_j is fed to g^k if and only if $\pi^k(c_j) \geq 0.5$ for $k \in [0, K]$.

3.1.2 NEURO-SYMBOLIC INTERPRETABLE MODELS

In this stage for the iteration k , we design interpretable model g^k to *interpret* the Blackbox f^{k-1} from the previous iteration $k-1$ by optimizing the following loss function,

$$\mathcal{L}_{(g^k, \pi^k)}^k(x_j, c_j) = \underbrace{\ell(f^{k-1}(x_j), g^k(c_j))\pi^k(c_j)}_{\text{trainable component for current iteration } k} \underbrace{\prod_{i=1}^{k-1} (1 - \pi^i(c_j))}_{\text{fixed component trained in the previous iterations}} \quad (3)$$

The term multiplied by the loss function ℓ in equation 3, is the probability of sample x_j reaching the interpretable model g^k , which is the probability of going through the residual for iterations 0 through $k-1$ (i.e. $\prod_{i=1}^{k-1} (1 - \pi^i(c_j))$) times the probability of going through the interpretable model at iteration k (i.e. $\pi^k(c_j)$). Refer to Figure 1 for an illustration. Note that π^1, \dots, π^{k-1} are learned in the previous iterations and are not trainable at iteration k . As each interpretable model g^k specializes in explaining a specific subset of samples (denoted by coverage τ), we refer to it as an *expert* moving forward. We adopted the optimization strategy, discussed in Geifman & El-Yaniv (2019) to optimize equation 2. We discuss the loss function in equation 3 in detail in Appendix A.2. After training, we refer to the interpretable experts of all the iterations as a ‘‘Mixture of Interpretable Experts’’ (MoIE) cumulatively.

3.1.3 THE RESIDUALS

The last step is to *repeat* with the residual r^k , as $r^k(x_j, c_j) = f^{k-1}(x_j) - g^k(c_j)$, to generate f^k , effectively making a new Blackbox for the next iteration $k+1$. Specifically, we train $f^k = h^k(\phi(\cdot))$ to match the residual r^k . This step is crucial to make f^k specialize over those samples not covered by g^k . For the k^{th} iteration, we optimize the following loss function to obtain f^k :

$$\mathcal{L}_f^k(x_j, c_j) = \underbrace{\ell(r^k(x_j, c_j), f^k(x_j))}_{\text{trainable component for iteration } k} \underbrace{\prod_{i=1}^k (1 - \pi^i(c_j))}_{\text{non-trainable component for iteration } k} \quad (4)$$

Notice that the embedding $\Phi(\cdot)$ is fixed for all the iterations. Due to computational reasons, we only update the last few layers of the Blackbox (h^k) in order to train f^k . At the final iteration K , our method yeilds a MoIE, explaining the interpretable component of the initial Blackbox f^0 and the final residual for the uninterpretable component of f^0 . Algorithm 1 in Appendix A.3 explains the training procedure of our model and extraction of FOL to explain samples locally. Figure 7 in Appendix A.3 shows the architecture of our model at inference.

4 EXPERIMENTS

To validate MoIE, we utilize four datasets - 1) bird species classification using CUB-200 Wah et al. (2011) dataset, 2) animals species classification using Animals with Attributes2 (Awa2) dataset Xian et al. (2018), 3) skin lesion classification using HAM10000 dataset Tschandl et al. (2018), 4) E-fusion and Cardiomegaly classification from radiology images using MIMIC-CXR dataset Johnson et al.. First, we conduct qualitative analysis to illustrate that MoIE captures variations in local and global explanations. Second, we demonstrate that MoIE does not compromise the performance of the Blackbox. Third, we validate that the performance of the residuals decreases over successive iterations as they cover ‘‘harder’’ instances. Finally, we leverage the Waterbirds dataset Sagawa et al. (2019) to eliminate the shortcut bias. In all the experiments, we repeat our method until at least 85% of samples are covered or the final residual’s accuracy (AUROC) falls below 70%. (0.7).

Training configurations As a Blackbox, we use ResNet-101 He et al. (2016) and Vision Transformer (ViT) Wang et al. (2021) for each of the CUB-200 and Awa2 datasets. For HAM10000 and MIMIC-CXR, we utilize Inception Szegedy et al. (2015) and Densenet-121 Huang et al. (2017) as the same. For CUB-200, we employ six experts each for both ViT and ResNet-based Blackboxes. For Awa2, we utilize 4 and 6 experts for ResNet-101 and ViT, respectively. For HAM10000 and MIMIC-CXR (for both Cardiomegaly and Effusion), we use 6 and 3 experts, respectively. Refer to Appendix A.1 and A.6 for details about the dataset and hyperparameters.

4.1 BASELINE

Our baseline is based on the *interpretable by design* principle, consisting of two parts: 1) a concept extractor $\phi : \mathcal{X} \rightarrow \mathcal{C}$, a mapping from the image to the concept space; and 2) $g : \mathcal{C} \rightarrow \mathcal{Y}$, a mapping from the concepts to the prediction. We train ϕ and g sequentially from scratch with the supervision of the human attributes \mathcal{C} and class labels \mathcal{Y} respectively. The concept extractor ϕ for Resnet, Inception, and Densenet121 includes all layers until the last convolution block. The ViT-based ϕ consists of the transformer encoder block (excluding the classification head). We use the identical configurations for g as described in Appendix A.6 for each dataset.

4.2 RESULTS

4.2.1 LOCAL EXPLANATIONS BY MOIE

Flexibility of local explanations Figure 2 compares the FOL explanations by different experts with the baseline. As the baseline includes a single interpretable model g , all the FOLs for each sample per class incorporate identical concepts. For example, the baseline utilizes *longneck*, *smelly*, *longleg* and *buckteeth* to identify all the samples of “Horse”. MoIE employs the concepts on a per-sample basis, so different experts adopt different concepts to classify the samples of a particular class. In Figure 2 the expert4 uses *smelly*, but the expert5 uses *fields* and *longneck* to distinguish the samples of “Horse”. MoIE demonstrates similar flexibility in creating the FOL explanation for HAM10000. According to figure 2 expert4 relies on *Blue Whitish Veils (BWV)*, *Irregular Streaks*, *Regular* and *Irregular Dots and Globules (DG)* to identify “Malignancy”, whereas expert6 utilizes *Irregular Dots and Globules* and *ATypical Pigment Net*. Appendices A.7.5 and A.7.6 display all the unique local FOLs for Awa2 and HAM10000 datasets respectively.

Flexibility of global explanations We perform the same analysis for CUB-200 to formulate a global explanation of a class by combining the different local FOLs per sample using *disjunctive normal form* (DNF) as in E-Lens. Figure 3 depicts such global explanations for the species “Bay-breasted warbler” by three distinct experts. Here we capture the heterogeneity in class-level explanations since each FOL corresponding to an expert has an amalgamation of distinct and shared concepts. For instance *leg_color_grey* is unique to expert4, but *belly_pattern_solid* and *back_pattern_multicolored* are unique to experts 1 and 2, respectively. Furthermore, *back_pattern_stripped* is shared by all FOLs by the three experts to identify “Bay-breasted warbler”. Appendix A.7.4 display more instances of such global explanations.

4.2.2 QUANTITATIVE ANALYSIS OF MOIE WITH THE BLACKBOX AND BASELINE

Figure 4 displays the performance of our method using a heldout test set. “MoIE” and “MoIE + Residual” denote the mixture of interpretable experts (g) excluding and including the final residual, respectively. Coverage (Cov in the figure) represents the proportion of samples in the test set covered by all the experts throughout iterations. For CUB-200, Awa2, and HAM10000, MoIE achieves similar performance to the Blackbox. For CUB-200 and HAM10000, our method achieves a significant performance gain compared to the baseline. For Awa2, the baseline performs at par with our model. (ResNet-based baseline exceeds ours). Note that all the datasets include noisy concepts except Awa2 (Awa2 is created for zero-shot learning), making it appropriate for the *interpretable by design* models. In general, ViT-derived experts performed better than their ResNet-based counterparts. The MIMIC-CXR dataset is highly imbalanced, with the positive samples being too few compared to the negative ones. As a result, the baselines for them attain similar accuracy scores as our MoIE model (Figure 4a). Therefore, precision and recall are better metrics for assessing the

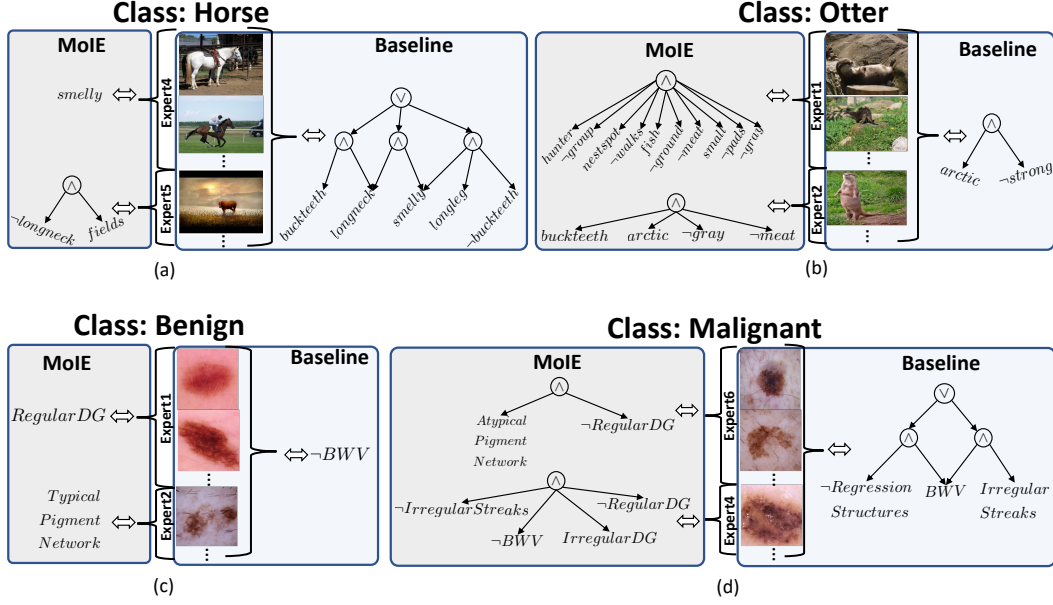


Figure 2: Illustration of flexibility of FOL explanations by MoIE. We report the FOL for different experts and the baseline to identify (a) Horse (b) Otter (c) Benign lesion and (d) Malignant lesion. For example in figure (a), the FOL by the baseline constitutes *longneck*, *smelly*, *longleg* and *buckteeth* concepts to distinguish all the samples of class “Horse”. However in the same figure (a), expert4 identifies the instances of “Horse” in the first two rows with *smelly* as the identifying concept. Similarly expert5 classifies the samples of “Horse” in the third row of figure (a) using *longneck* and *fields*. Importantly, *longneck* and *smelly* are shared by the baseline and the experts.

models’ performance on these datasets. To demonstrate this, we plot the AUROC in Figure 4b. As it can be seen, MoIE significantly outperforms the baseline in terms of AUROC.

4.2.3 PERFORMANCE OF EACH EXPERT AND THE RESIDUAL

Figure 5 displays the proportional accuracy of MoIE and the residual for the CUB-200 and Awa2 datasets. Proportional accuracy of each model (experts and/or residuals) is defined as the accuracy of that model times its coverage. Recall that the model’s coverage is the empirical mean of the samples selected by the selector. The dashed line in each of the plots indicates the performance of the blackbox, f^0 , denoting the upper bound of our MoIE models. As shown in Figure 5a, the VIT-derived expert and residual cumulatively achieve an accuracy of approximately 91% for the CUB-200 dataset in iteration 1, where the residual’s contribution (black bar) is greater than the expert1’s (blue bar). Later iterations reveal that the MoIE’s performances cumulatively increase, and the residual worsens. In the final iteration, the MoIE contributes most to performance as they carve out all the interpretable segments from the Blackbox. We observe that the final uninterpretable samples that are routed towards the final residual are “harder” samples for the model to predict, resulting in a lower residual accuracy. Tracing these samples back to f^0 , we observe that the original blackbox has a similar low performance for predicting these samples. Figures 5 and Table 6 in the Appendix verifies this claim. We have shown some of these “hard” images side by side with the ones explained by the experts for CUB-200 in Appendix A.7.8. Per our investigation and as it can be in the images, “hard” examples tend to be blurry or distorted images or ones with birds not fully centered or hard to tell from the background.

As shown in the coverage plot, this experiment reinforces figure 1, where the flow through the experts gradually becomes thicker compared to the narrower flow of the residual with every iteration. We observe similar trends for the other architectures and datasets. For medical imaging (HAM and MIMIC-CXR) datasets and ResNet-derived experts of vision datasets, refer to figures 11 and 10 in the Appendix A.7.3 and A.7.2, respectively.

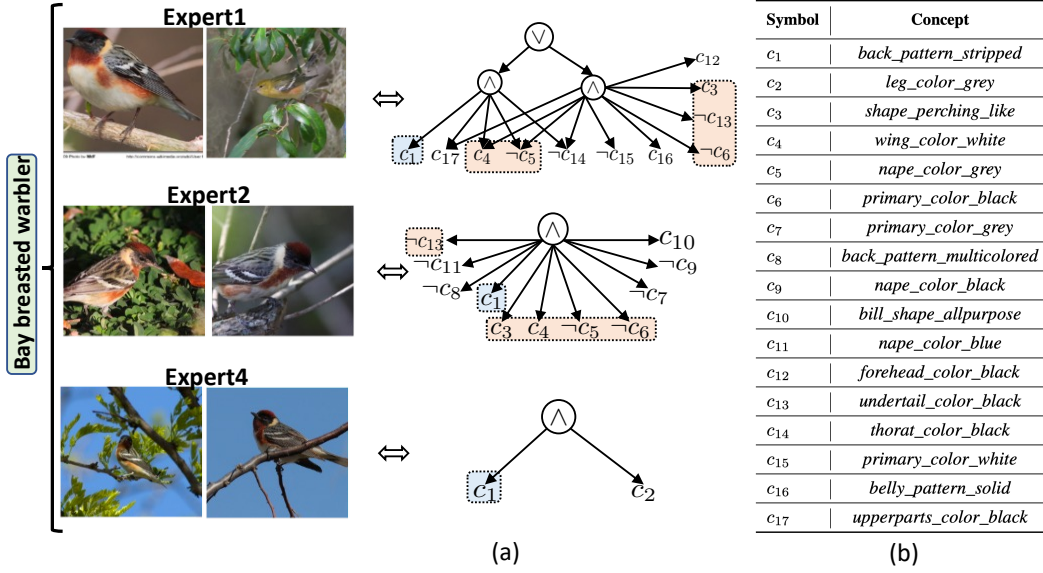


Figure 3: Illustration of class-level or **global** explanations. We report the global explanation of a bird species, “Bay breasted warbler” using the VIT-based blackbox by combining (using disjunctive normal form (DNF)) the local explanations. (a) Explanations of “Bay breasted warbler” by expert1 (top row), expert2 (middle row) and expert4 (bottom row). Shared concepts across all the experts are highlighted in *blue*. We highlight the same for experts 1 and 2 in *orange*. (b) Symbols used in figure 3a and their corresponding true concept labels.

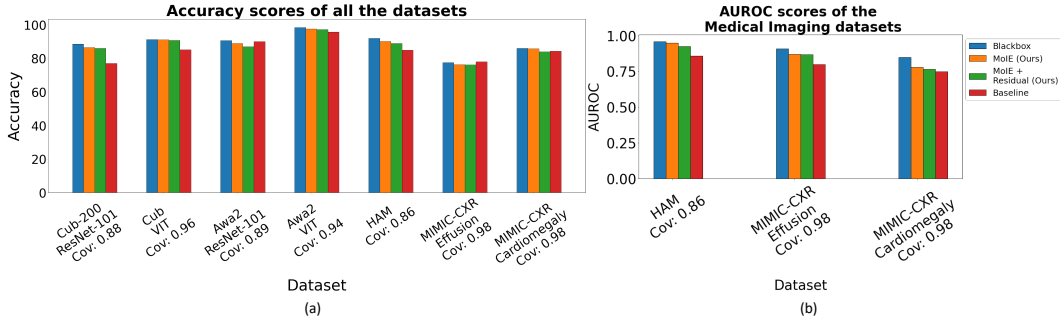


Figure 4: MoIE does not hurt the performance of the Blackbox. From left to right, we compare the (a) Accuracy and (b) AUROC metrics respectively. For the MoIE (ours) in the figure, we specify the empirical coverage as *Cov* w.r.t each datasets.

4.3 APPLICATION IN REMOVAL OF SHORTCUTS

To conduct this experiment, we create the Waterbirds dataset as in Sagawa et al. (2019) by spuriously correlating the images of birds from the Caltech-UCSD Birds-200-2011 dataset to the images of land and water background from the Places dataset. Specifically, we use forest and bamboo as the spurious land concepts for landbirds; ocean and lakes as the spurious water concepts for waterbirds. Thus, we have 112 visual concepts (108 concepts from CUB-200 and four new concepts for the background). We aim to identify each bird as a Waterbird or a Landbird. We use ResNet50 (He et al. (2016)) as the Blackbox f^0 . The Blackbox quickly latches on the spurious background to classify the birds. As a result, the black box’s accuracy varies for land-based subsets versus aquatic subsets of the bird species, as shown in figure 6a. The Waterbird on water is more accurate than on land (96% vs. 67 % in the orange bar in the figure 6a). We train t to retrieve the concepts from the biased Blackbox. Next, we train our MoIE to explain the bird species using FOL. As per figure 6c (middle row), the FOL of a waterbird misclassified as a landbird captures the spurious concept *forest*. Assuming the background concepts as metadata, we aim to reduce the background bias from the representation

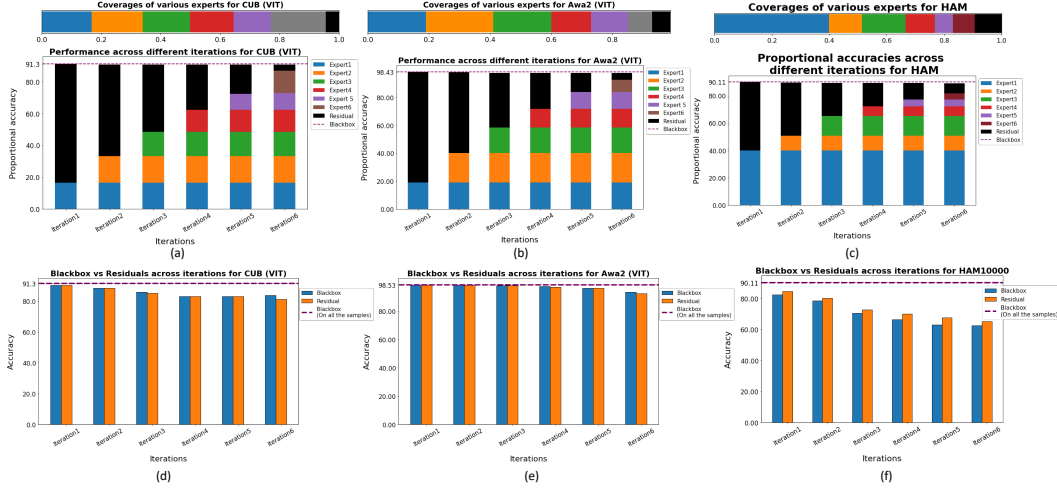


Figure 5: Illustration of experts across iterations. (a) - (c). Coverage and relative performance of the individual experts and residuals for each iteration. We route the samples covered by the residuals across iterations to the initial blackbox f^0 and compare the accuracy of f^0 (blue bar) with the residual (orange bar) for the each dataset in (d)-(f). Figures d-f show that the residuals perform poorly at the later iterations, covering the “harder” samples (orange bar). This claim is substantiated by the similar abysmal performance of the initial blackbox f^0 (blue bar) on the same instances covered by the respective residual. As a result, the contribution of the residuals to the cumulative performance of MoIE worsens (black regions figures a-c).

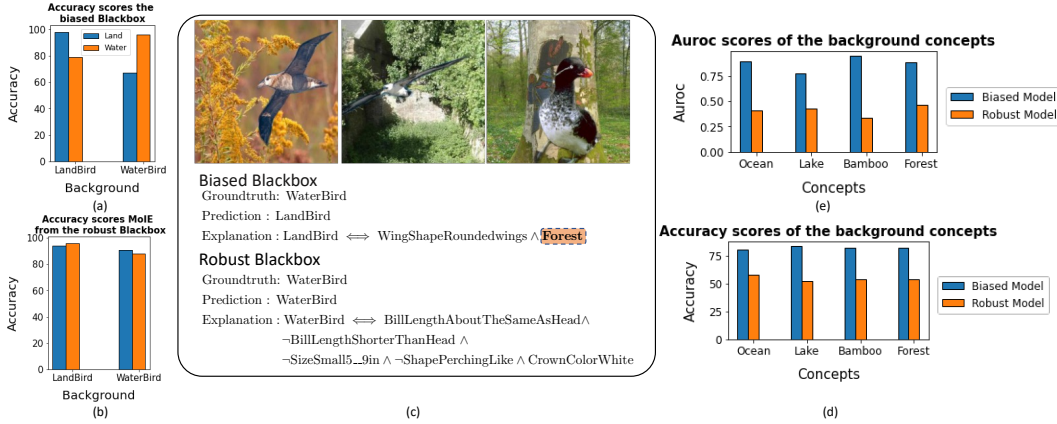


Figure 6: Applying MoIE to eliminate shortcuts. (a) Performance of the biased Blackbox. (b) Performance of final MoIE, trained using the supervision of the robust Blackbox after removing the shortcuts using MDN. (c) Examples of samples and their explanations by the biased (top-row) and robust Blackboxes (bottom-row). (d) auroc and (e) accuracy metrics of the biased Blackbox (when the shortcuts are present) and the robust Blackbox (when the shortcuts are removed using MDN).

of the Blackbox using metadata normalization (MDN) Lu et al. (2021). Therefore, we leverage the MDN layers between two successive layers of the convolutional backbone to fine-tune the biased Blackbox. Next, we train t , using the embedding ϕ of the robust Blackbox. Figures 6d-e compare the auroc and accuracy scores of the spurious background concepts from the embedding ϕ of the biased and robust Blackboxes, respectively. The validation auroc (accuracy) of all the spurious concepts retrieved from the robust Blackbox fell well short of the predefined threshold 0.7 (70 %) compared to the biased Blackbox. Finally, we re-train the MoIE distilling from the new robust Blackbox. Figure 6b illustrates that the accuracies of Waterbird on water vs. Waterbird on land become pretty similar (91% -88 %). The FOL from the robust Blackbox does not include any background concepts (Figure 6c, bottom row). Refer to the figure 8 in Appendix A.5 for the flow diagram of this experiment.

5 DISCUSSION & CONCLUSIONS

This paper proposes a novel method to iteratively extract a mixture of interpretable models from a trained Blackbox by utilizing the flexibility of the Blackbox to bridge the gap between post hoc explanation and the construction of interpretable models. The comprehensive experiments on a various datasets demonstrate that 1) our model maintains a similar performance compared to the Blackbox while making it explainable, 2) the local explanations by our model account for the diversity of explanations of the various samples in a dataset, 3) the coverage of the residuals gradually declines over the iterations. Finally, we employ our method to eliminate the shortcuts in images effectively. In the future we aim to apply our method to other modalities such as text or video.

REFERENCES

- Abubakar Abid, Mert Yuksekgonul, and James Zou. Meaningfully explaining model mistakes using conceptual counterfactuals. *arXiv preprint arXiv:2106.12723*, 2021.
- Julius Adebayo, Justin Gilmer, Michael Muelly, Ian Goodfellow, Moritz Hardt, and Been Kim. Sanity checks for saliency maps. *Advances in neural information processing systems*, 31, 2018.
- Raed Alharbi, Minh N Vu, and My T Thai. Learning interpretation with explainable knowledge distillation. In *2021 IEEE International Conference on Big Data (Big Data)*, pp. 705–714. IEEE, 2021.
- Pietro Barbiero, Gabriele Ciravegna, Francesco Giannini, Pietro Lió, Marco Gori, and Stefano Melacci. Entropy-based logic explanations of neural networks. In *Proceedings of the AAAI Conference on Artificial Intelligence*, volume 36, pp. 6046–6054, 2022.
- L Breiman, J Friedman, CJ Stone, and RA Olshen. Classification and regression trees (crc, boca raton, fl). 1984.
- Chaofan Chen, Oscar Li, Daniel Tao, Alina Barnett, Cynthia Rudin, and Jonathan K Su. This looks like that: deep learning for interpretable image recognition. *Advances in neural information processing systems*, 32, 2019.
- Xu Cheng, Zhefan Rao, Yilan Chen, and Quanshi Zhang. Explaining knowledge distillation by quantifying the knowledge. In *Proceedings of the IEEE/CVF conference on computer vision and pattern recognition*, pp. 12925–12935, 2020.
- Gabriele Ciravegna, Pietro Barbiero, Francesco Giannini, Marco Gori, Pietro Lió, Marco Maggini, and Stefano Melacci. Logic explained networks. *arXiv preprint arXiv:2108.05149*, 2021.
- Roxana Daneshjou, Kailas Vodrahalli, Weixin Liang, Roberto A Novoa, Melissa Jenkins, Veronica Rotemberg, Justin Ko, Susan M Swetter, Elizabeth E Bailey, Olivier Gevaert, et al. Disparities in dermatology ai: Assessments using diverse clinical images. *arXiv preprint arXiv:2111.08006*, 2021.
- Yonatan Geifman and Ran El-Yaniv. Selectivenet: A deep neural network with an integrated reject option. In *International conference on machine learning*, pp. 2151–2159. PMLR, 2019.
- Trevor Hastie and Robert Tibshirani. Generalized additive models: some applications. *Journal of the American Statistical Association*, 82(398):371–386, 1987.
- Kaiming He, Xiangyu Zhang, Shaoqing Ren, and Jian Sun. Deep residual learning for image recognition. In *Proceedings of the IEEE conference on computer vision and pattern recognition*, pp. 770–778, 2016.
- Geoffrey Hinton, Oriol Vinyals, Jeff Dean, et al. Distilling the knowledge in a neural network. *arXiv preprint arXiv:1503.02531*, 2(7), 2015.
- Gao Huang, Zhuang Liu, Laurens Van Der Maaten, and Kilian Q Weinberger. Densely connected convolutional networks. In *Proceedings of the IEEE conference on computer vision and pattern recognition*, pp. 4700–4708, 2017.

-
- Saahil Jain, Ashwin Agrawal, Adriel Saporta, Steven QH Truong, Du Nguyen Duong, Tan Bui, Pierre Chambon, Yuhao Zhang, Matthew P Lungren, Andrew Y Ng, et al. Radgraph: Extracting clinical entities and relations from radiology reports. *arXiv preprint arXiv:2106.14463*, 2021.
- Alistair Johnson, Matt Lungren, Yifan Peng, Zhiyong Lu, Roger Mark, Seth Berkowitz, and Steven Horng. Mimic-cxr-jpg-chest radiographs with structured labels.
- Jeremy Kawahara, Sara Daneshvar, Giuseppe Argenziano, and Ghassan Hamarneh. Seven-point checklist and skin lesion classification using multitask multimodal neural nets. *IEEE journal of biomedical and health informatics*, 23(2):538–546, 2018.
- Been Kim, Martin Wattenberg, Justin Gilmer, Carrie Cai, James Wexler, Fernanda Viegas, and Rory Sayres. Interpretability beyond feature attribution: Quantitative testing with concept activation vectors (tcav).(2017). *arXiv preprint arXiv:1711.11279*, 2017.
- Pieter-Jan Kindermans, Sara Hooker, Julius Adebayo, Maximilian Alber, Kristof T Schütt, Sven Dähne, Dumitru Erhan, and Been Kim. The (un) reliability of saliency methods. In *Explainable AI: Interpreting, Explaining and Visualizing Deep Learning*, pp. 267–280. Springer, 2019.
- Pang Wei Koh, Thao Nguyen, Yew Siang Tang, Stephen Mussmann, Emma Pierson, Been Kim, and Percy Liang. Concept bottleneck models. In *International Conference on Machine Learning*, pp. 5338–5348. PMLR, 2020.
- Benjamin Letham, Cynthia Rudin, Tyler H McCormick, and David Madigan. Interpretable classifiers using rules and bayesian analysis: Building a better stroke prediction model. *The Annals of Applied Statistics*, 9(3):1350–1371, 2015.
- Mandy Lu, Qingyu Zhao, Jiequan Zhang, Kilian M Pohl, Li Fei-Fei, Juan Carlos Niebles, and Ehsan Adeli. Metadata normalization. In *Proceedings of the IEEE/CVF Conference on Computer Vision and Pattern Recognition*, pp. 10917–10927, 2021.
- Adriano Lucieri, Muhammad Naseer Bajwa, Stephan Alexander Braun, Muhammad Imran Malik, Andreas Dengel, and Sheraz Ahmed. On interpretability of deep learning based skin lesion classifiers using concept activation vectors. In *2020 international joint conference on neural networks (IJCNN)*, pp. 1–10. IEEE, 2020.
- Scott M Lundberg and Su-In Lee. A unified approach to interpreting model predictions. In *Proceedings of the 31st international conference on neural information processing systems*, pp. 4768–4777, 2017.
- Grégoire Montavon, Wojciech Samek, and Klaus-Robert Müller. Methods for interpreting and understanding deep neural networks. *Digital signal processing*, 73:1–15, 2018.
- Marco Tulio Ribeiro, Sameer Singh, and Carlos Guestrin. " why should i trust you?" explaining the predictions of any classifier. In *Proceedings of the 22nd ACM SIGKDD international conference on knowledge discovery and data mining*, pp. 1135–1144, 2016.
- Cynthia Rudin. Stop explaining black box machine learning models for high stakes decisions and use interpretable models instead. *Nature Machine Intelligence*, 1(5):206–215, 2019.
- Shiori Sagawa, Pang Wei Koh, Tatsunori B Hashimoto, and Percy Liang. Distributionally robust neural networks for group shifts: On the importance of regularization for worst-case generalization. *arXiv preprint arXiv:1911.08731*, 2019.
- Wojciech Samek, Alexander Binder, Grégoire Montavon, Sebastian Lapuschkin, and Klaus-Robert Müller. Evaluating the visualization of what a deep neural network has learned. *IEEE transactions on neural networks and learning systems*, 28(11):2660–2673, 2016.
- Ramprasaath R Selvaraju, Michael Cogswell, Abhishek Das, Ramakrishna Vedantam, Devi Parikh, and Dhruv Batra. Grad-cam: Visual explanations from deep networks via gradient-based localization. In *Proceedings of the IEEE international conference on computer vision*, pp. 618–626, 2017.

-
- Avanti Shrikumar, Peyton Greenside, Anna Shcherbina, and Anshul Kundaje. Not just a black box: Learning important features through propagating activation differences. *arXiv preprint arXiv:1605.01713*, 2016.
- Karen Simonyan, Andrea Vedaldi, and Andrew Zisserman. Deep inside convolutional networks: Visualising image classification models and saliency maps. *arXiv preprint arXiv:1312.6034*, 2013.
- Sumedha Singla, Brian Pollack, Junxiang Chen, and Kayhan Batmanghelich. Explanation by progressive exaggeration. *arXiv preprint arXiv:1911.00483*, 2019.
- Daniel Smilkov, Nikhil Thorat, Been Kim, Fernanda Viégas, and Martin Wattenberg. Smoothgrad: removing noise by adding noise. *arXiv preprint arXiv:1706.03825*, 2017.
- Christian Szegedy, Wei Liu, Yangqing Jia, Pierre Sermanet, Scott Reed, Dragomir Anguelov, Dumitru Erhan, Vincent Vanhoucke, and Andrew Rabinovich. Going deeper with convolutions. In *Proceedings of the IEEE conference on computer vision and pattern recognition*, pp. 1–9, 2015.
- Philipp Tschandl, Cliff Rosendahl, and Harald Kittler. The ham10000 dataset, a large collection of multi-source dermatoscopic images of common pigmented skin lesions. *Scientific data*, 5(1):1–9, 2018.
- David Wadden, Ulme Wennberg, Yi Luan, and Hannaneh Hajishirzi. Entity, relation, and event extraction with contextualized span representations. In *Proceedings of the 2019 Conference on Empirical Methods in Natural Language Processing and the 9th International Joint Conference on Natural Language Processing (EMNLP-IJCNLP)*, pp. 5784–5789, Hong Kong, China, November 2019. Association for Computational Linguistics. doi: 10.18653/v1/D19-1585. URL <https://aclanthology.org/D19-1585>.
- Catherine Wah, Steve Branson, Peter Welinder, Pietro Perona, and Serge Belongie. The caltech-ucsd birds-200-2011 dataset. 2011.
- Charles Wan, Rodrigo Belo, and Leid Zejnilovic. Explainability’s gain is optimality’s loss? how explanations bias decision-making. In *Proceedings of the 2022 AAAI/ACM Conference on AI, Ethics, and Society*, pp. 778–787, 2022.
- Jun Wang, Xiaohan Yu, and Yongsheng Gao. Feature fusion vision transformer for fine-grained visual categorization. *arXiv preprint arXiv:2107.02341*, 2021.
- Yongqin Xian, Christoph H Lampert, Bernt Schiele, and Zeynep Akata. Zero-shot learning—a comprehensive evaluation of the good, the bad and the ugly. *IEEE transactions on pattern analysis and machine intelligence*, 41(9):2251–2265, 2018.
- Ke Yu, Shantanu Ghosh, Zhexiong Liu, Christopher Deible, and Kayhan Batmanghelich. Anatomy-guided weakly-supervised abnormality localization in chest x-rays. *arXiv preprint arXiv:2206.12704*, 2022.
- Mert Yuksekogonul, Maggie Wang, and James Zou. Post-hoc concept bottleneck models. *arXiv preprint arXiv:2205.15480*, 2022.

A APPENDIX

A.1 DATASETS

CUB-200 The Caltech-UCSD Birds-200-2011 (Wah et al. (2011)) is a fine-grained classification dataset comprising 11788 images and 312 noisy visual concepts. The aim is to classify the correct bird species from 200 possible classes. We adopted the strategy discussed in Koh et al. (2020) to extract 108 denoised visual concepts. Also, we utilize training/validation splits shared in Barbiero et al. (2022). Finally, we use the state-of-the-art classification models Resnet-101 (He et al. (2016)) and Vision-Transformer (ViT) (Wang et al. (2021)) as the blackboxes f .

Animals with attributes2 (Awa2) Awa2 dataset Xian et al. (2018) consists of 37322 images of total 50 animals classes with 85 numeric attribute. We aim to classify the correct animal species from 200 possible classes. We use the state-of-the-art classification models Resnet-101 (He et al. (2016)) and Vision-Transformer (ViT) (Wang et al. (2021)) as the blackboxes f .

HAM10000 HAM10000 (Tschandl et al. (2018)) is a classification dataset aiming to classify a skin lesion benign or malignant. Following Daneshjou et al. (2021), we use Inception Szegedy et al. (2015) model, trained on this dataset as the blackbox f . We follow the strategy in Lucieri et al. (2020) to extract the 9 concepts from the Derm7pt (Kawahara et al. (2018)) dataset.

MIMIC-CXR We use 220,763 frontal images from the MIMIC-CXR dataset Johnson et al. aiming to classify cardiomegaly and effusion. We obtain the anatomical and observation concepts from the RadGraph annotations in RadGraph’s inference dataset (Jain et al. (2021)), automatically generated by DYGIE++ (Wadden et al. (2019)). We use the test-train-validation splits from Yu et al. (2022) and Densenet121 Huang et al. (2017) as the blackbox f .

A.2 LOSS FUNCTION

In this section, we will discuss the loss function used in distilling the knowledge from the blackbox to the symbolic model. We remove the superscript k for brevity. We adopted the optimization proposed in Geifman & El-Yaniv (2019). Specifically, we convert the constrained optimization problem in equation 2 as

$$\begin{aligned}\mathcal{L}_s &= \mathcal{R}(\pi, g) + \lambda_s \Psi(\tau - \zeta(\pi)) \\ \Psi(a) &= \max(0, a)^2,\end{aligned}\tag{5}$$

where τ is the target coverage and λ_s is a hyperparameter (Lagrange multiplier). We define $\mathcal{R}(\cdot)$ and $\mathcal{L}_{g,\pi}(\cdot)$ in equations 1 and 3 respectively. ℓ in equation 3 is defined as follows:

$$\ell(f, g) = \ell_{\text{distill}}(f, g) + \lambda_{\text{len}} \sum_{i=1}^r \mathcal{H}(\beta^i),\tag{6}$$

where λ_{len} and $\mathcal{H}(\beta^i)$ are the hyperparameters and entropy regularize, introduced in Barbiero et al. (2022) with r being the total number of class labels. Specifically, β^i is the categorical distribution of the weights corresponding to each concept. To select only a few relevant concepts for each target class, higher values of λ_{len} will lead to a sparser configuration of β . ℓ is the knowledge distillation loss Hinton et al. (2015), defined as

$$\begin{aligned}\ell(f, g) &= (\alpha_{KD} * T_{KD} * T_{KD}) KL(\text{LogSoftmax}(g(\cdot)/T_{KD}), \text{Softmax}(f(\cdot)/T_{KD})) + \\ &\quad (1 - \alpha_{KD}) CE(g(\cdot), y),\end{aligned}\tag{7}$$

where T_{KD} is the temperature, CE is the Cross-Entropy loss, and α_{KD} is relative weighting controlling the supervision from the blackbox f and the class label y .

As discussed in Geifman & El-Yaniv (2019), we also define an auxiliary interpretable model using the same prediction task assigned to g using the following loss function

$$\mathcal{L}_{aux} = \frac{1}{m} \sum_{j=1}^m \ell_{distill}(f(\mathbf{x}_j), g(\mathbf{c}_j)) + \lambda_{lens} \sum_{i=1}^r \mathcal{H}(\beta^i), \quad (8)$$

which is agnostic of any coverage. \mathcal{L}_{aux} is necessary for optimization as the symbolic model will focus on the target coverage τ before learning any relevant features, overfitting to the wrong subset of the training set. The final loss function to optimize by g in each iteration is as follows:

$$\mathcal{L} = \alpha \mathcal{L}_f + (1 - \alpha) \mathcal{L}_{aux}, \quad (9)$$

where α can be tuned as a hyperparameter. Following Geifman & El-Yaniv (2019), we also use $\alpha = 0.5$ in all of our experiments.

A.3 ALGORITHM

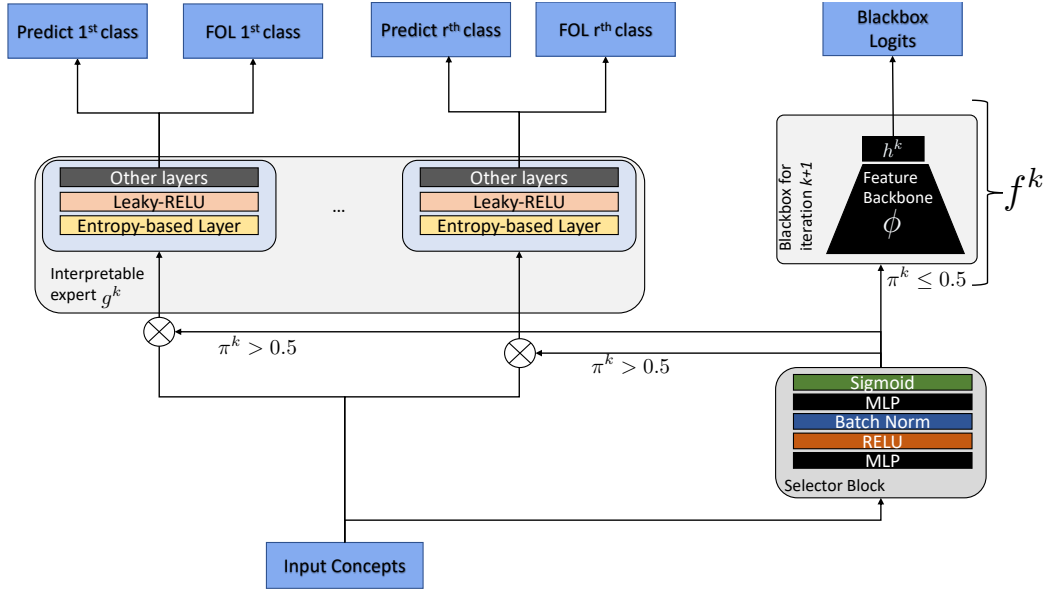


Figure 7: Architecture of MoIE. In an iteration k during inference, the selector routes the samples to go through the interpretable expert g^k if the probability $\pi^k \geq 0.5$. If $\pi^k < 0.5$, the selector routes the samples, through f^k , the Blackbox for iteration $k + 1$. Note $f^k = h^k(\phi(\cdot))$ is an approximation of the residual $r^k = f^{k-1} - g^k$.

Algorithm 1 explains the overall training procedure of our method. Figure 7 displays the architecture of our model in iteration k .

A.4 CODE AVAILABILITY

We will upload the code upon the decision from the reviewers.

A.5 FLOW DIAGRAM TO ELIMINATE SHOTCUT

Figure 8 shows the flow diagram to eliminate shortcut.

Algorithm 1 Training the MoIE to generate FOL explanations locally.

Input: Training set: $\{\mathcal{X}, \mathcal{Y}, \mathcal{S}\}$; trained blackbox $f^0 = h^0(\phi(\cdot))$ using supervision of \mathcal{Y} ; K as the # iterations; Coverages τ_1, \dots, τ_k

Output: Sparse mixture of experts and their selectors $\{g^k, \pi^k\}_{k=1}^K$,

- 1: Fix ϕ .
 - 2: Train t by minimizing $\text{BinaryCrossEnt}(t(\phi(x), \mathcal{S}))$
 - 3: Form a concept bank \mathcal{C} with p concepts after discarding the concepts whose validation auROC (accuracy) ≤ 0.7 (70%)
 - 4: **for** iteration $k = 1 \dots K$ **do**
 - 5: Fix $\pi^1 \dots \pi^{k-1}$.
 - 6: Minimize \mathcal{L}^k using equation 9 to learn π^k and g^k .
 - 7: Calculate $r^k = f^{k-1}(\cdot) - g^k(\cdot)$
 - 8: Minimize equation 4 to learn $f^k(\cdot)$, the new blackbox for the next iteration $k + 1$
 - 9: **end for**
 - 10: **for** experts $k = 1 \dots K$ **do**
 - 11: **for** each sample in the test-set **do**
 - 12: Sort the concepts according to their attention scores from different experts in descending order.
 - 13: Initialise FOL_bucket as empty list.
 - 14: Select one concept $\{c^i\}_{i=1}^p$ at a time from the sorted concept bank in step 12 until $g(c^i) = g(c)$ and add those concepts in the FOL_bucket.
 - 15: Construct the FOL expression from FOL_bucket using Barbiero et al. (2022).
 - 16: **end for**
 - 17: **end for**
-

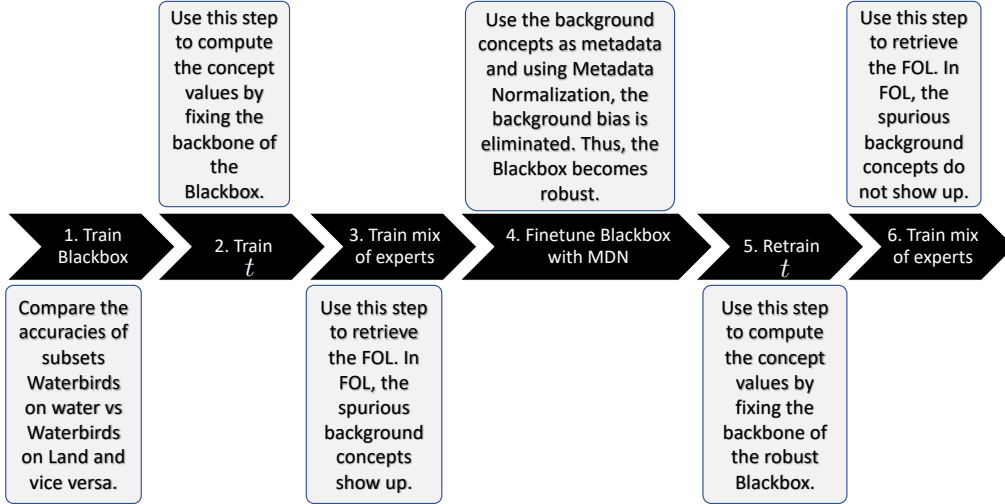


Figure 8: The flow diagram to eliminate the shortcut from vision datasets using FOL by MoIE.

A.6 ARCHITECTURAL DETAILS OF SYMBOLIC EXPERTS AND HYPERPARAMETERS

Table 1 demonstrates different settings to train the Blackbox of CUB-200, Awa2 and MIMIC-CXR respectively. For the ViT-based backbone, we used the same hyperparameter setting used in the state-of-the-art ViT-B_16 variant in Wang et al. (2021). To train t , we flatten the feature maps from the last convolutional block of ϕ using “Adaptive average pooling” for CUB-200 and Awa2 datasets. For MIMIC-CXR and HAM10000, we flatten out the feature maps from the last convolutional block. For ViT-based backbones, we take the first block of representation from the encoder of ViT. For HAM10000, we use the same Blackbox in Yuksekogonul et al. (2022). Tables 2, 3, 4, 5 enumerate all the different settings to train the interpretable experts for CUB-200, Awa2, HAM, and MIMIC-CXR respectively. All the residuals in different iterations follow the same settings as their blackbox counterparts. Furthermore, we only include concepts as input to g if their validation

Table 1: Hyperparameter setting of different convolution-based Blackboxes used by CUB-200, Awa2 and MIMIC-CXR

Setting	CUB-200	Awa2	MIMIC-CXR
Backbone	ResNet-101	ResNet-101	DenseNet-121
Pretrained on ImageNet	True	True	True
Image size	448	224	448
Learning rate	0.001	0.001	0.01
Optimization	SGD	Adam	SGD
Weight-decay	0.00001	0	0.0001
Epcchs	95	90	50
Layers used as ϕ	till 4 th ResNet Block	till 4 th ResNet Block	till 4 th DenseNet Block
Flattening type for the input to t	Adaptive average pooling	Adaptive average pooling	Flatten

accuracy or auroc exceeds a certain threshold (in all of our experiments, we fix 0.7 or 70% as the threshold of validation auroc or accuracy). For HAM10000, we use the identical “concept bank” as proposed in Yuksekgonul et al. (2022).

Table 2: Hyperparameter setting of interpretable experts (g) trained on ResNet-101 (top) and VIT (bottom) blackboxes for the CUB-200 dataset

Settings based on dataset	Iteration 1	Iteration 2	Iteration 3	Iteration 4	Iteration 5	Iteration 6
CUB-200 (ResNet-101)						
+ Batch size	16	16	16	16	16	16
+ Coverage (τ)	0.2	0.2	0.2	0.2	0.2	0.2
+ Learning rate	0.01	0.01	0.01	0.01	0.01	0.01
+ λ_{lens}	0.0001	0.0001	0.0001	0.0001	0.0001	0.0001
+ α_{KD}	0.9	0.9	0.9	0.9	0.9	0.9
+ T_{KD}	10	10	10	10	10	10
+hidden neurons	10	10	10	10	10	10
+ λ_s	32	32	32	32	32	32
+ Temperature						
E-Lens (T_{lens})	0.7	0.7	0.7	0.7	0.7	0.7
CUB-200 (VIT)						
+ Batch size	16	16	16	16	16	16
+ Coverage (τ)	0.2	0.2	0.2	0.2	0.2	0.2
+ Learning rate	0.01	0.01	0.01	0.01	0.01	0.01
+ λ_{lens}	0.0001	0.0001	0.0001	0.0001	0.0001	0.0001
+ α_{KD}	0.99	0.99	0.99	0.99	0.99	0.99
+ T_{KD}	10	10	10	10	10	10
+hidden neurons	10	10	10	10	10	10
+ λ_s	32	32	32	32	32	32
+ Temperature						
E-Lens (T_{lens})	6.0	6.0	6.0	6.0	6.0	6.0

Table 3: Hyperparameter setting of interpretable experts (g) trained on ResNet-101 (top) and VIT (bottom) blackboxes for the Awa2 dataset

Settings based on dataset	Iteration 1	Iteration 2	Iteration 3	Iteration 4	Iteration 5	Iteration 6
Awa2 (ResNet-101)						
+ Batch size	30	30	30	30	-	-
+ Coverage (τ)	0.4	0.35	0.35	0.25	-	-
+ Learning rate	0.001	0.001	0.001	0.001	-	-
+ λ_{lens}	0.0001	0.0001	0.0001	0.0001	-	-
+ α_{KD}	0.9	0.9	0.9	0.9	-	-
+ T_{KD}	10	10	10	10	-	-
+hidden neurons	10	10	10	10	-	-
+ λ_s	32	32	32	32	-	-
+ Temperature						
E-Lens (T_{lens})	0.7	0.7	0.7	0.7	-	-
Awa2 (VIT)						
+ Batch size	30	30	30	30	30	30
+ Coverage (τ)	0.2	0.2	0.2	0.2	0.2	0.2
+ Learning rate	0.01	0.01	0.01	0.01	0.01	0.01
+ λ_{lens}	0.0001	0.0001	0.0001	0.0001	0.0001	0.0001
+ α_{KD}	0.99	0.99	0.99	0.99	0.99	0.99
+ T_{KD}	10	10	10	10	10	10
+hidden neurons	10	10	10	10	10	10
+ λ_s	32	32	32	32	32	32
+ Temperature						
E-Lens (T_{lens})	6.0	6.0	6.0	6.0	6.0	6.0

Table 4: Hyperparameter setting of interpretable experts (g) for the diseases - Effusion (top) and Cardiomegaly (bottom) in the dataset HAM10000

Settings based on dataset	Iteration 1	Iteration 2	Iteration 3	Iteration 4	Iteration 5	Iteration 6
HAM10000 (Inception-V3)						
+ Batch size	32	32	32	32	32	32
+ Coverage (τ)	0.4	0.2	0.2	0.2	0.2	0.2
+ Learning rate	0.01	0.01	0.01	0.01	0.01	0.01
+ λ_{lens}	0.0001	0.0001	0.0001	0.0001	0.0001	0.0001
+ α_{KD}	0.9	0.9	0.9	0.9	0.9	0.9
+ T_{KD}	10	10	10	10	10	10
+hidden neurons	10	10	10	10	10	10
+ λ_s	64	64	64	64	64	64
+ Temperature						
E-Lens (T_{lens})	0.7	0.7	0.7	0.7	0.7	0.7

A.7 MORE RESULTS

A.7.1 SUMMARY STATISTICS OF NO. OF CONCEPTS USED FOR VARIOUS ARCHITECTURES

Figure 9 shows the summary statistics for multiclass classification vision datasets. For both datasets, we observe that the VIT-based MoIE uses fewer concepts for explanation than their ResNet-based counterparts. For example, for the CUB-200 dataset, expert6 of VIT-backbone requires 25 concepts

Table 5: Hyperparameter setting of interpretable experts (g) for the dataset MIMIC-CXR

Settings based on dataset	Iteration 1	Iteration 2	Iteration 3
Effusion-MIMIC-CXR (DenseNet-121)			
+ Batch size	64	64	64
+ Coverage (τ)	0.5	0.2	0.1
+ Learning rate	0.01	0.01	0.01
+ λ_{lens}	0.0001	0.0001	0.0001
+ α_{KD}	0.99	0.99	0.99
+ T_{KD}	20	20	20
+hidden neurons	20, 20	20, 20	20, 20
+ λ_s	96	128	256
+ Temperature			
E-Lens (T_{lens})	7.6	7.6	7.6
Cardiomegaly-MIMIC-CXR (DenseNet-121)			
+ Batch size	64	64	64
+ Coverage (τ)	0.5	0.15	0.1
+ Learning rate	0.01	0.01	0.01
+ λ_{lens}	0.0001	0.0001	0.0001
+ α_{KD}	0.99	0.99	0.99
+ T_{KD}	20	20	20
+hidden neurons	20, 20	20, 20	20, 20
+ λ_s	1024	64	256
+ Temperature			
E-Lens (T_{lens})	0.7	0.7	0.7

compared to 105 by expert6 of ResNet-101-backbone (Figure 9a). The 105 concepts by expert6 is the highest number of concepts utilized by any expert for CUB-200. Similarly, for Awa2, the highest number concept used by an expert is 8 for the ViT-based backbone compared to 80 for the ResNet-101-based backbone(Figure 9b).

A.7.2 PERFORMANCE OF EXPERTS AND RESIDUAL FOR RESNET-DERIVED EXPERTS OF AWA2 AND CUB-200 DATASETS

Figure 10 shows the coverage (top row), performances (bottom row) of each expert and residual for the ResNet-101-derived experts of Awa2 and CUB-200 dataset respectively.

A.7.3 PERFORMANCE OF EXPERTS AND RESIDUAL FOR MEDICAL IMAGING DATASETS

Figure 11 shows the coverage (top row), auroc (middle row) and accuracy scores (bottom row) of each expert and residual for all the medical imaging datasets (HAM10000, Effusion of MIMIC-CXR and Cardiomegaly of MIMIC-CXR).

A.7.4 MORE RESULTS OF CUB DATASET

Figures 12, 13 and 14 display the average number of concepts required to predict a bird species correctly in the Cub-200 dataset for all the experts of ViT as backbones. Also, Figures 15, 17 and 17 display the same for the ResNet-101 based counterparts. As mentioned before, the average number of concepts for class $j = \frac{\sum \text{all concepts for the samples belong to class } j}{\# \text{ samples of class } j}$. We can see that for ResNet-101, on average 80 concepts are required to explain a sample correctly for the class “Rhinoceros_Auklet” (expert3 in Figure 17 a). However, for ViT, only 6 concepts are needed to explain a sample correctly “Rhinoceros_Auklet” (expert3 in Figure 17 a). From both of these figures, we can see that different experts require a different number of concepts to explain the same class. For example, figures 12 (b) and 14 (b) reveal that experts 2 and 6 require 25 and 58 concepts on average to explain “Arctic_Tern”

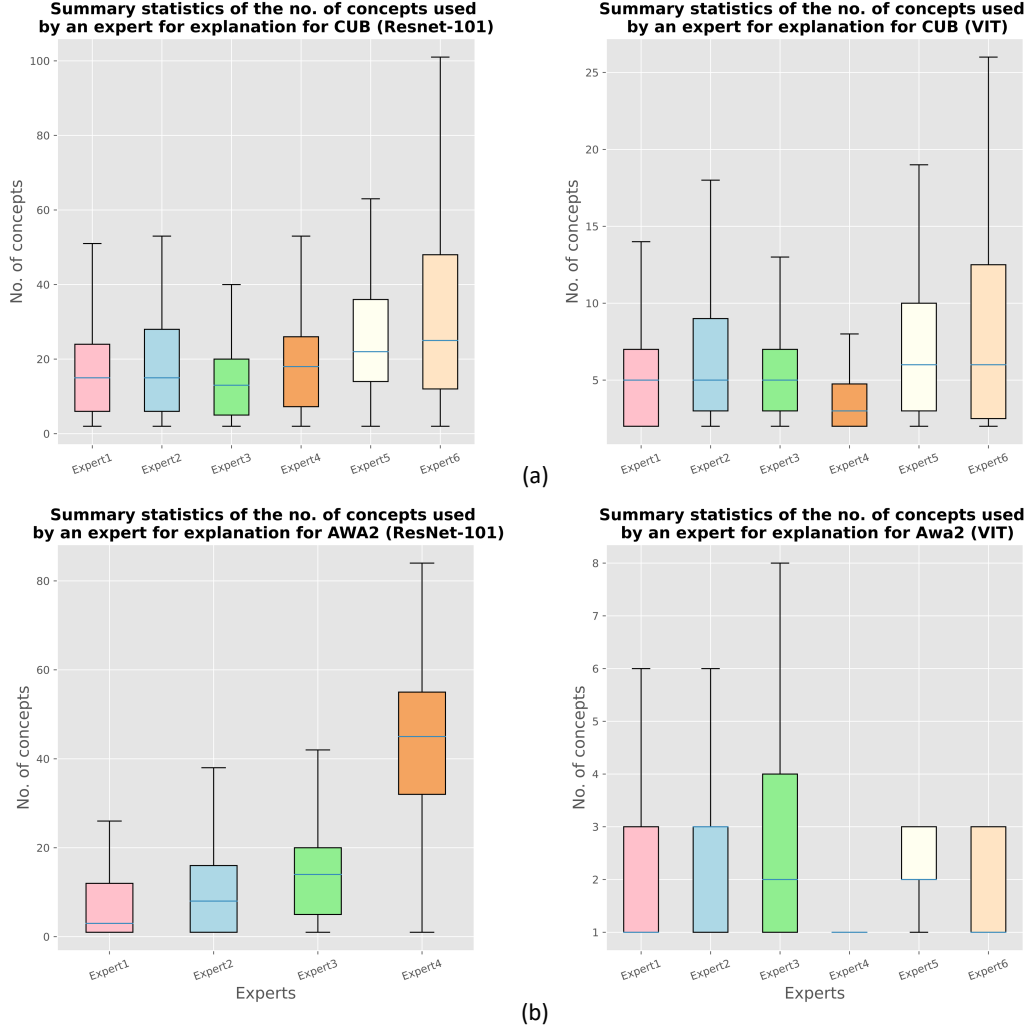


Figure 9: Summary statistics of the number of concepts utilized by various experts of datasets (a) CUB-200(top row) and (b) Awa2 (bottom row). In general, we can see that experts carving out the explanations from ViT often uses less number of concepts.

correctly respectively. Figures 18, 19, 20 show more results on global explanations of CUB-200 dataset.

A.7.5 RESULTS OF AWA2 DATASET

Figure 21, shows the various local explanations for different species of animals in the Awa2 dataset. For brevity, we choose a maximum of 4 images per class in this figure. If an expert only includes one sample, we only show the image of that sample in this figure. For example, expert4 relies on the *water* concept to predict a “Beaver”, whereas expert1 uses several other concepts such as *gray*, *nocturnal*, *muscle*. Figures 22 and 23 display the average number of concepts required to predict an animal species correctly in the Awa2 dataset for ResNet-101 and ViT as backbones, respectively. Specifically, the average number of concepts for class $j = \frac{\sum \text{all concepts for the samples belong to class } j}{\# \text{ samples of class } j}$. We can see that for ResNet-101, on average, 80 concepts are required to explain a sample correctly for the class “Weasel” (Expert1 in Figure 22 a). However, for ViT, only three concepts are needed to explain a sample correctly for “Weasel” (Expert 6 in Figure 23 f). Also from both of these figures 22 and 23, we can see that different experts require different number concepts to explain same class.

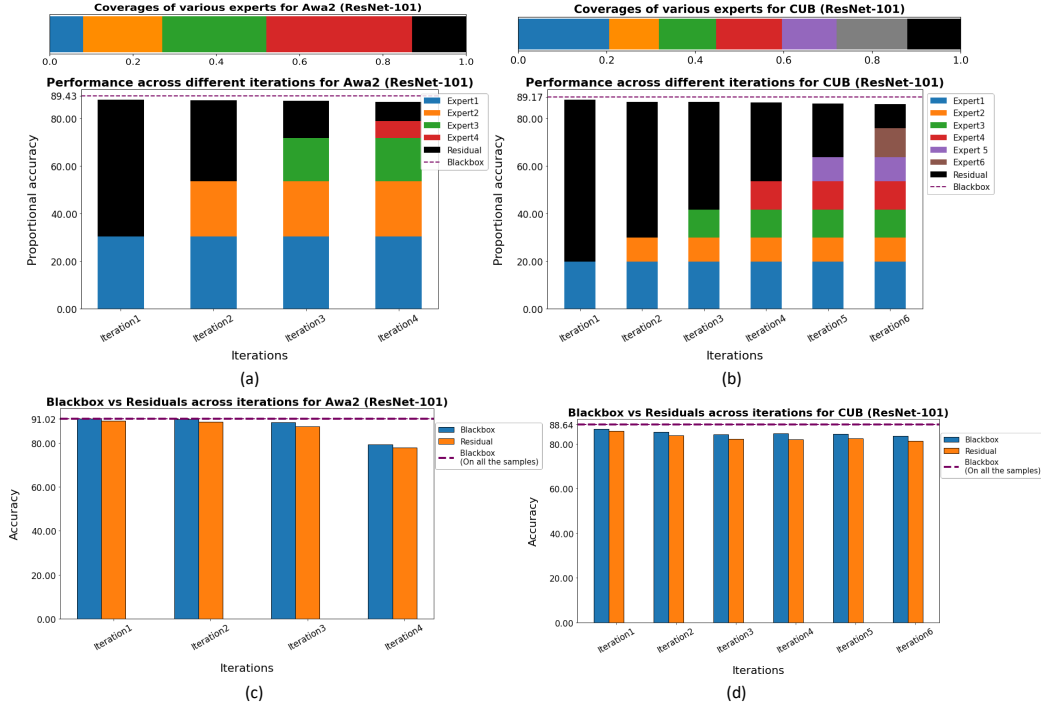


Figure 10: Coverage and performance of the experts and residual across iterations for the ResNet-101-derived experts of - (a) Awa2 and (b) CUB-200.

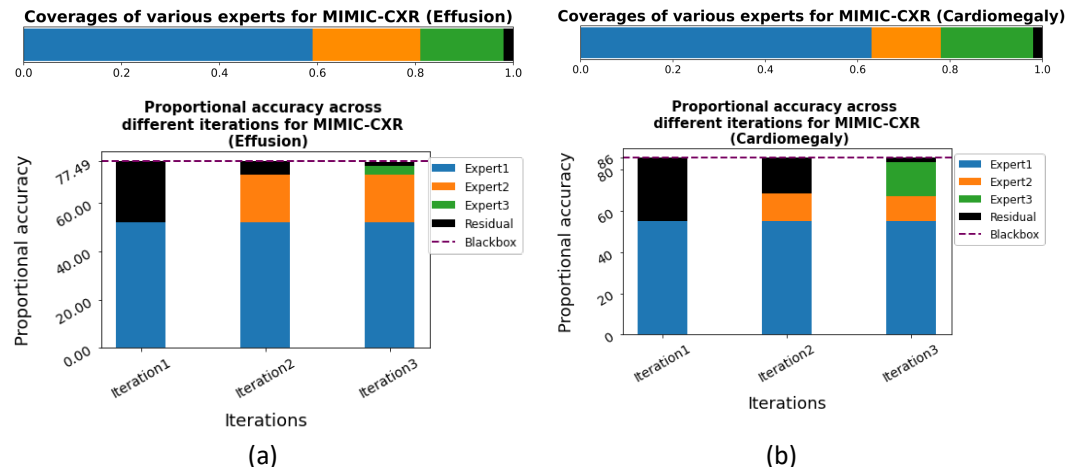


Figure 11: Coverage and performance of the experts and residual across iterations for all the medical imaging datasets - (a) HAM10000 (b) Effusion of MIMIC-CXR and (c) Cardiomegaly of MIMIC-CXR

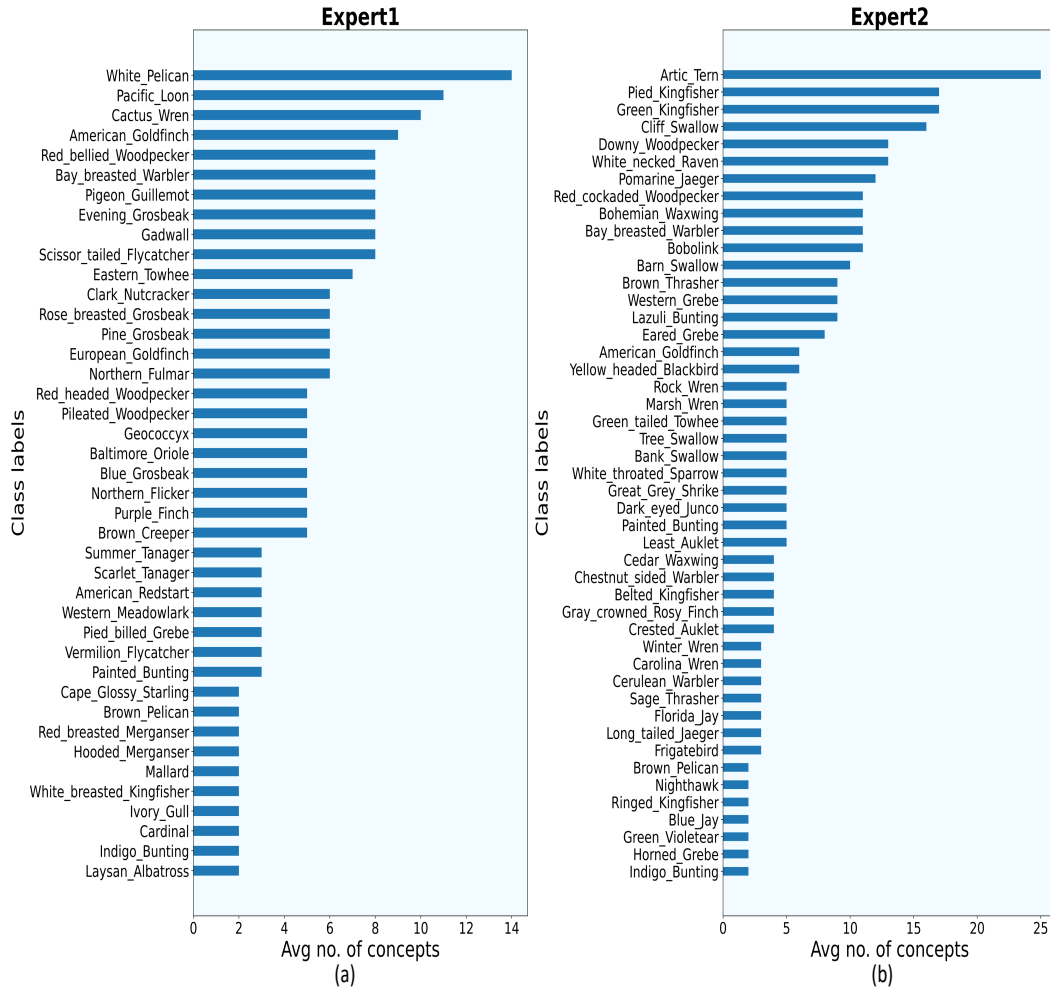


Figure 12: Class labels (Bird species) vs avg concepts using VIT as backbone for CUB-200 by (a) Expert1 (b) Expert2. Each bar in this plot indicates the average number concepts required to explain each sample of that bird species correctly. For example according to (a) expert1 requires 14 concepts to explain an instance of “White Pelican”.

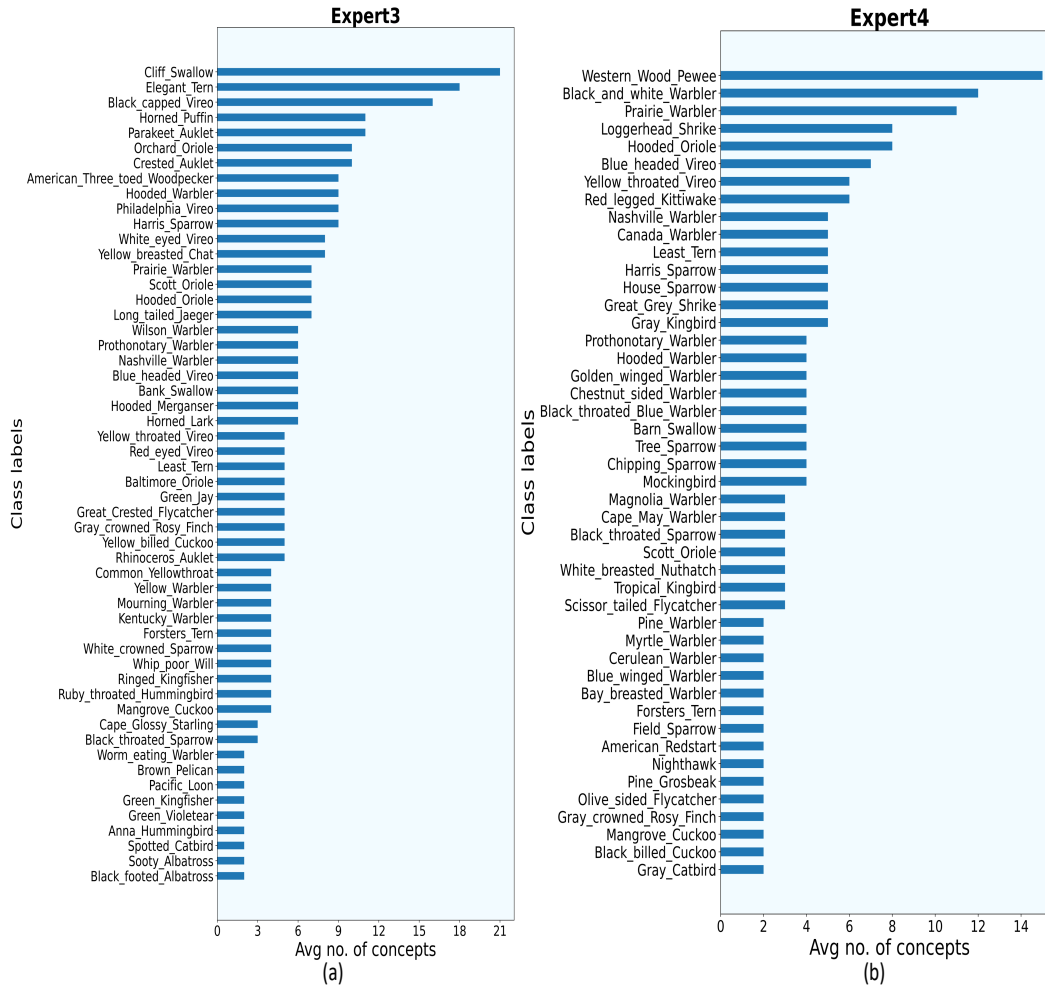


Figure 13: Class labels (Bird species) vs avg concepts using VIT as backbone for CUB-200 by (a) Expert3 (b) Expert4. Each bar in this plot indicates the average number concepts required to explain each sample of that bird species correctly. For example according to (a) expert3 requires 21 concepts to explain an instance of “Cliff Swallow”.

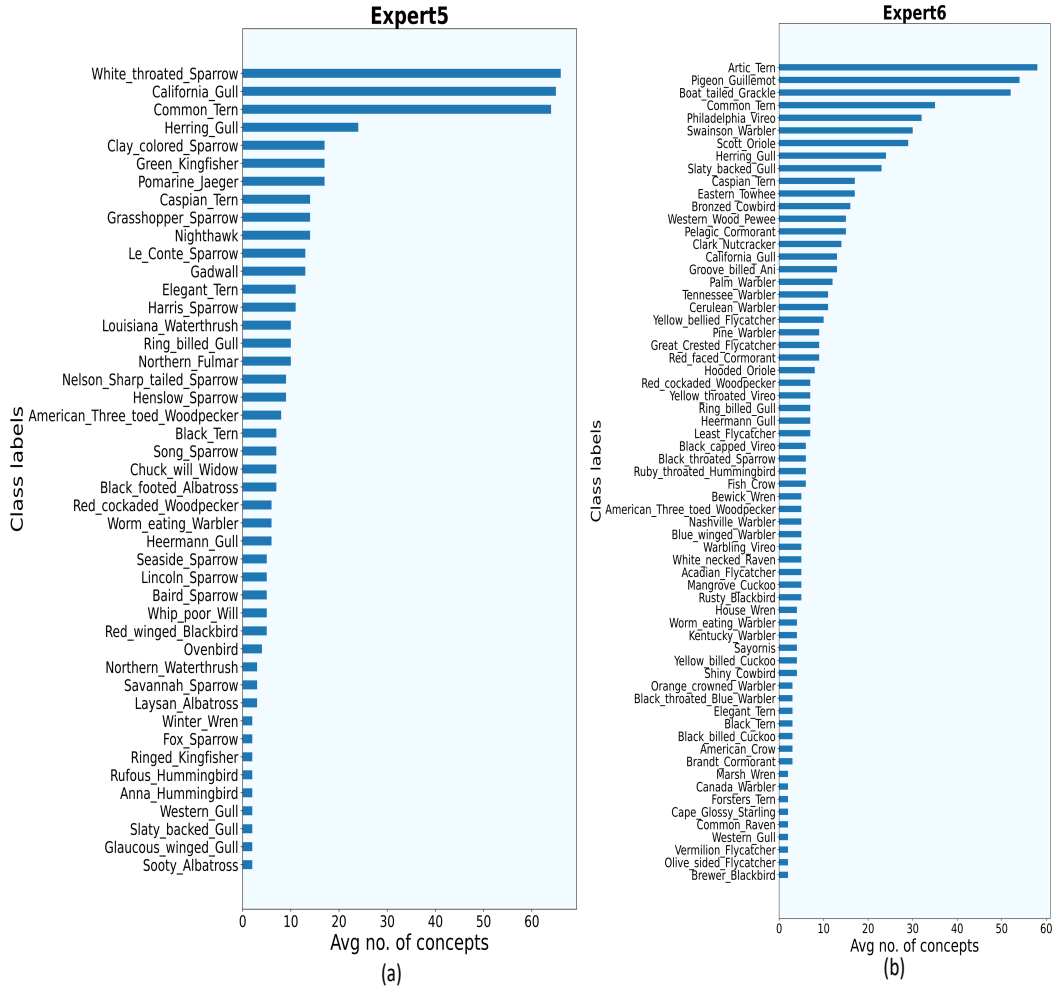


Figure 14: Class labels (Bird species) vs avg concepts using VIT as backbone for CUB-200 by (a) Expert5 (b) Expert6. Each bar in this plot indicates the average number concepts required to explain each sample of that bird species correctly. For example according to (a) expert5 requires approximately 65 concepts to explain an instance of “White throated sparrow”.

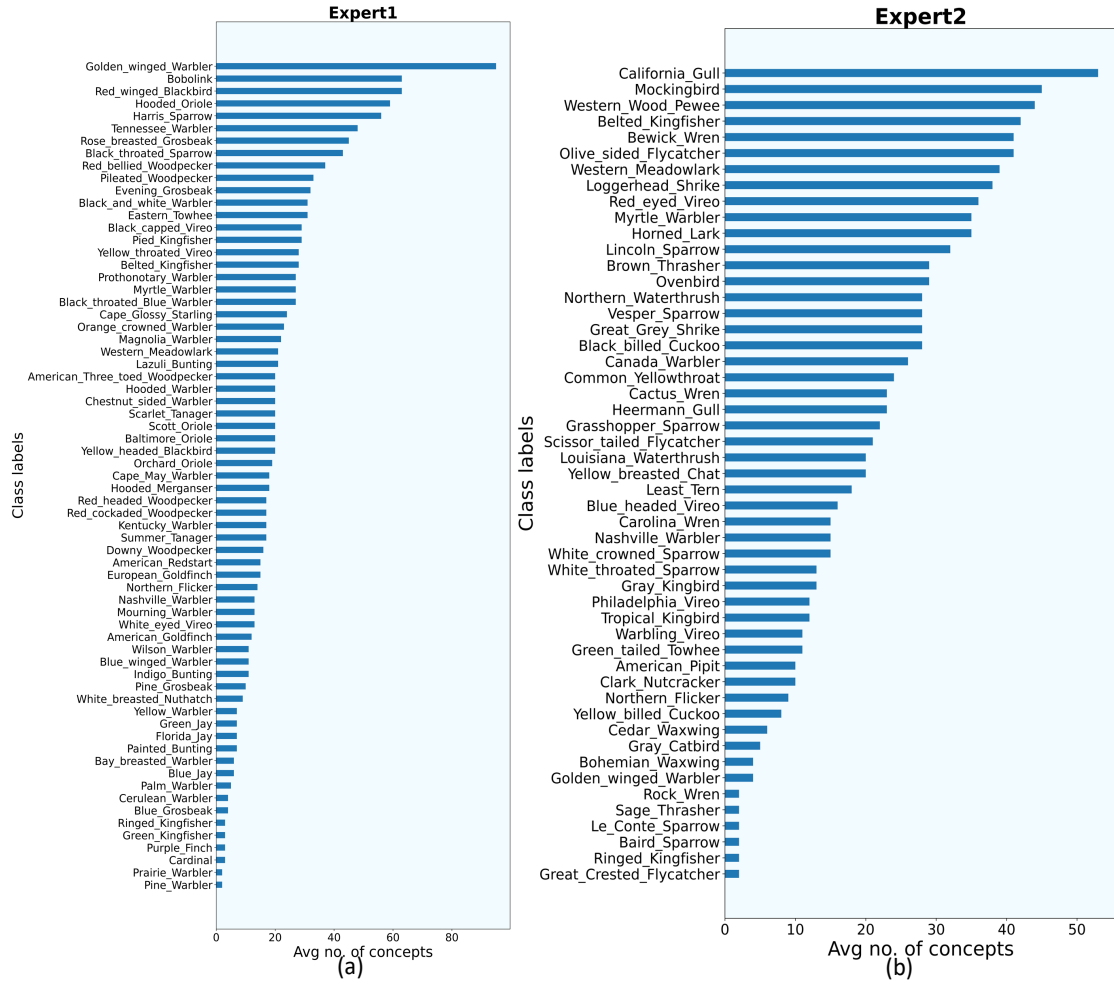


Figure 15: Class labels (Bird species) vs avg concepts using ResNet-101 as backbone for CUB-200 by (a) Expert1 (b) Expert2. Each bar in this plot indicates the average number concepts required to explain each sample of that bird species correctly. For example according to (a) expert1 requires approximately 85 concepts to explain an instance of “Golden winged warbler”.

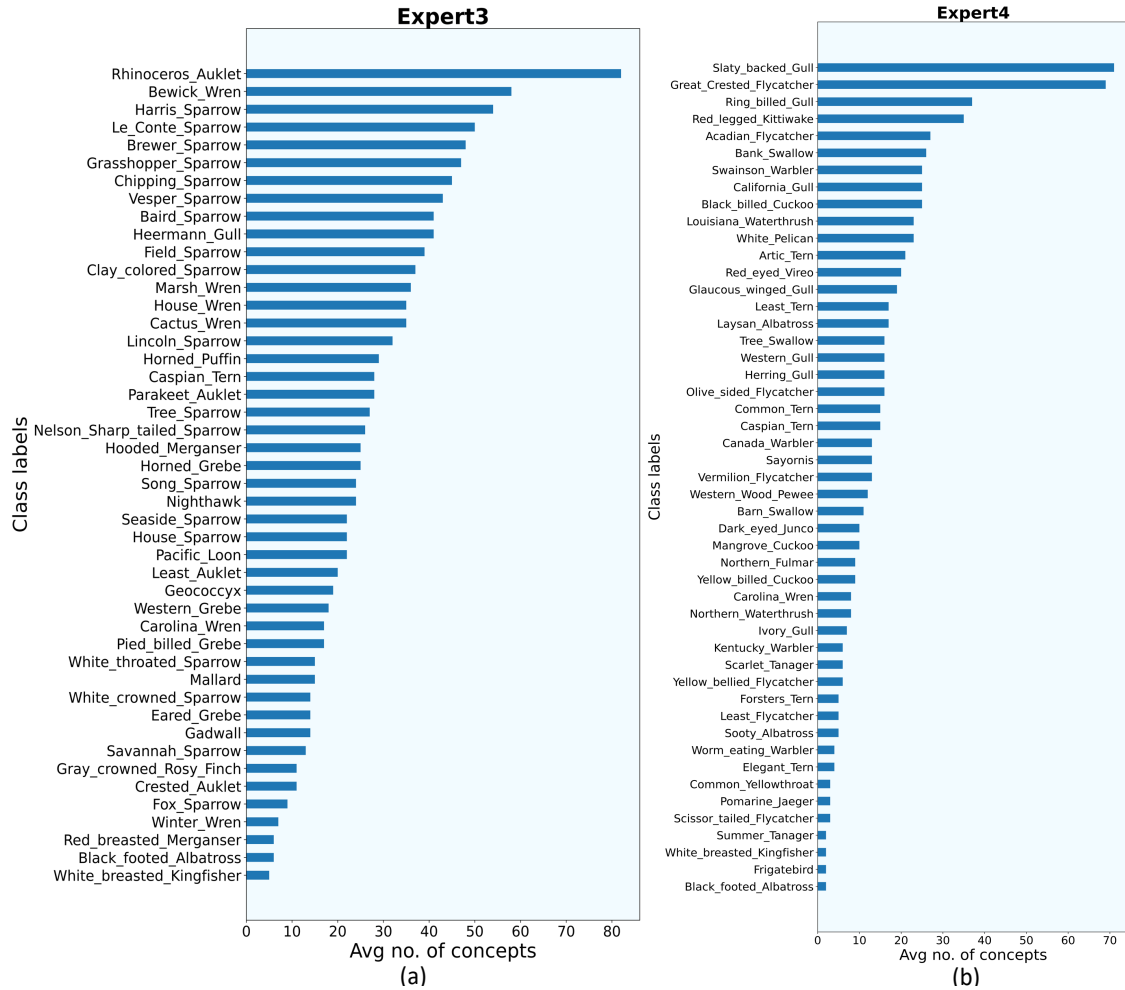


Figure 16: Class labels (Bird species) vs avg concepts using ResNet-101 as backbone for CUB-200 by (a) Expert3 (b) Expert4. Each bar in this plot indicates the average number concepts required to explain each sample of that bird species correctly. For example according to (a) expert3 requires approximately 82 concepts to explain an instance of “Rhinoceros auklet”.

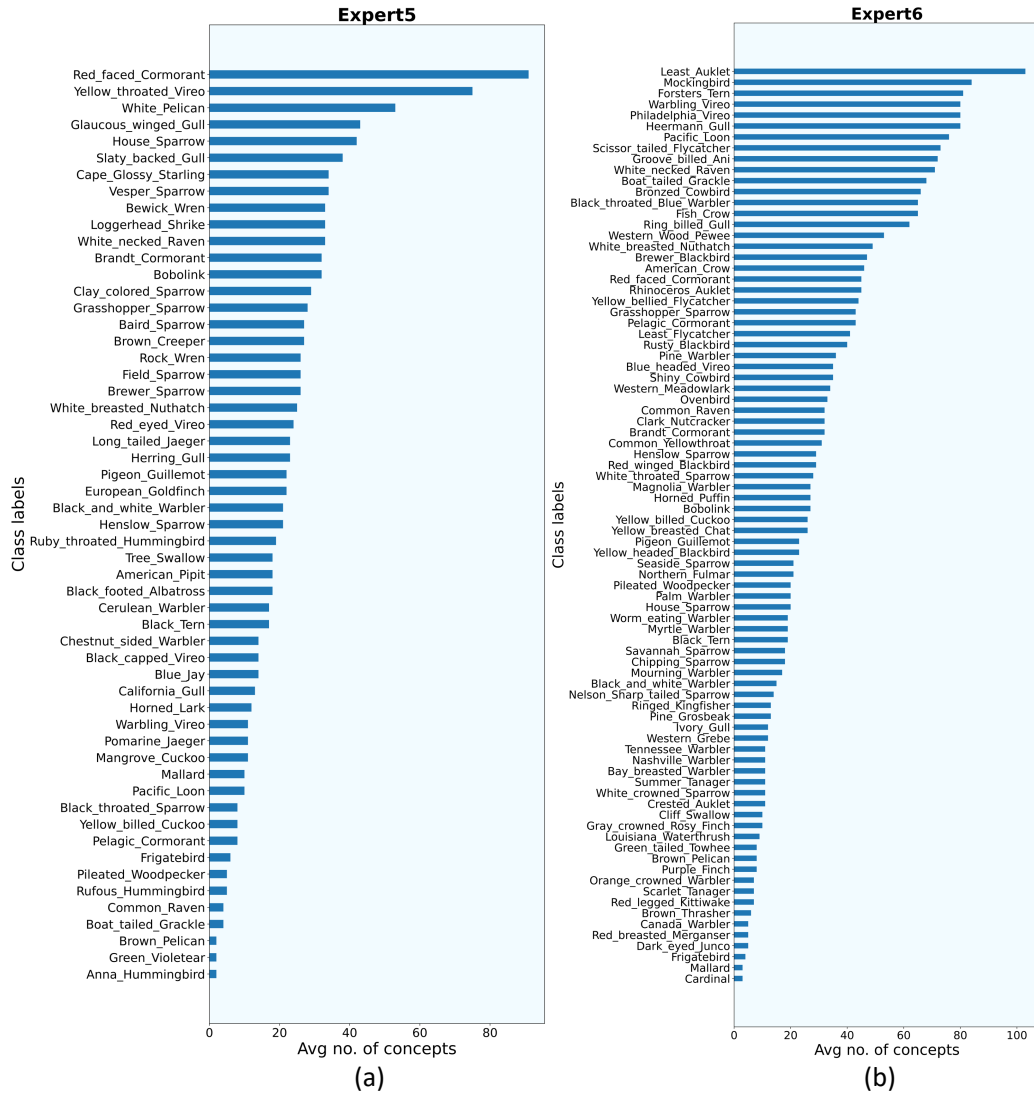


Figure 17: Class labels (Bird species) vs avg concepts using ResNet-101 as backbone for CUB-200 by (a) Expert5 (b) Expert6. Each bar in this plot indicates the average number concepts required to explain each sample of that bird species correctly. For example according to (a) expert5 requires approximately 85 concepts to explain an instance of “Red faced cormorant”.

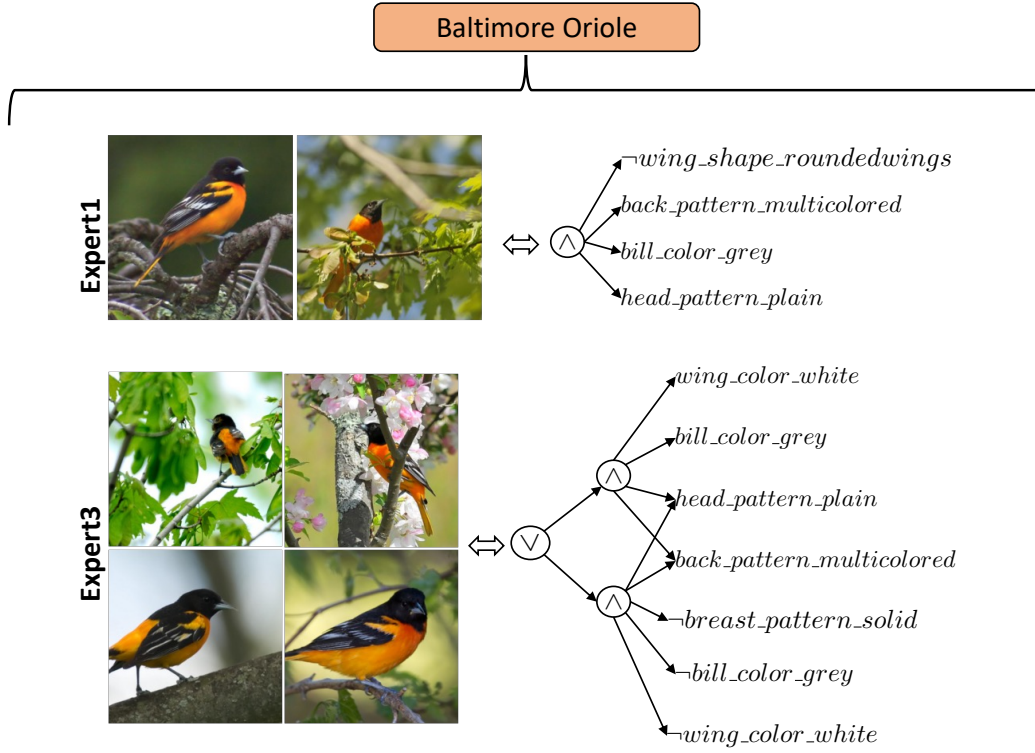


Figure 18: Generation of class-level explanations from VIT as a blackbox by combining the local explanations of “Baltimore Oriole Bunting” by expert1(top row) and expert3 (bottom row).

For example figures 23 (e) and (f) reveal that experts 5 and 6 require 4 and 30 concepts on average to explain “Wolf” correctly.

A.7.6 MORE RESULTS OF HAM1000 DATASET

Concept Importance As shown in E-Lens Barbiero et al. (2022), each expert constructs local FOL per sample, composing the concepts based on their attention weights. Figure 26 exhibit a quantitative analysis of the relative frequency of the concepts used by various experts to correctly classify the “Malignant” and “Benign” skin lesions, respectively. Also, expert4 (the yellow bars in the figure 26-bottom) classifies “Malignancy,” using multiple concepts, such as *IrregularStreaks*, *IrregularDG*, *Blue Whitish Veil (BWV)* etc., whereas expert3 (the grey bar in the figure 26-bottom) just utilizes *ATypical Pigment Network*.

Local FOL by MoIE Figures 24 and 25 displays all unique individual FOL explanations by various experts to predict the skin lesions as “Malignant” and “Benign” correctly. In this figure, we observe that expert1 relies solely on the concept *Regular Dots and Globules (RegularDG)* to classify a skin lesion as “Benign”, whereas expert3 relies on two different sets (one set consists of only *BWV*, and second one consists of *BWV*, *TypicalPigmentNetwork* etc.). This result substantiates our hypothesis that different experts rely on different concepts for different diseases unlike the baselines in figures 24a and 25a detecting a skin lesion as “Malignant” and “Benign” respectively.

A.7.7 RESULTS OF MIMIC-CXR DATASET

Figures 27 and 28 reveal the instances of local explanations for “Effusion” and “Cardiomegaly” respectively in MIMIC-CXR dataset.

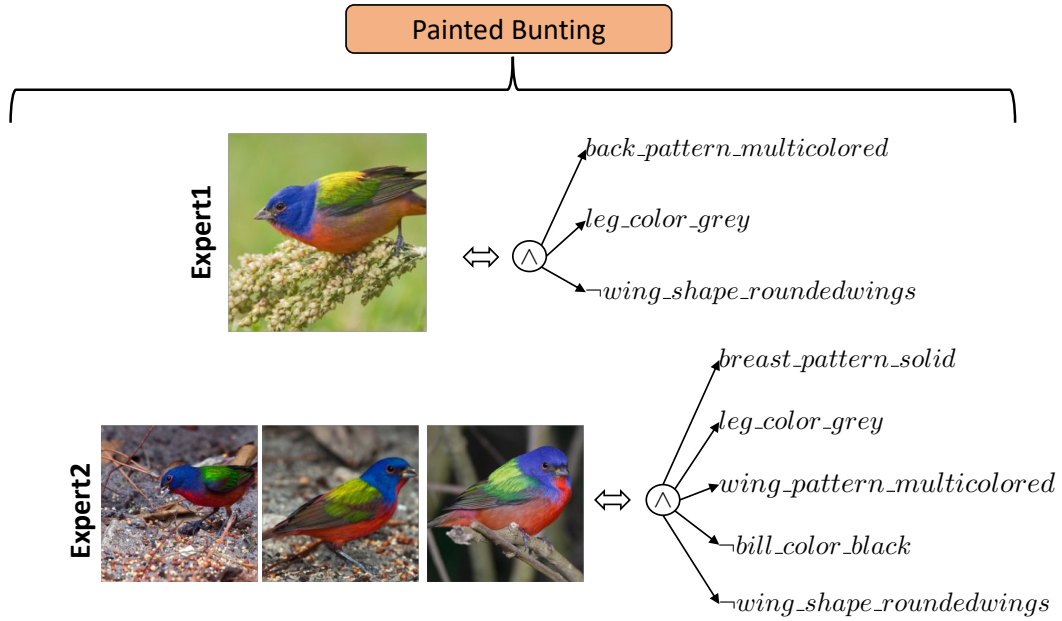


Figure 19: Generation of class-level explanations from VIT as a blackbox by combining the local explanations of “Painted Bunting” by expert1(top row) and expert2 (bottom row). Note that all the samples have same local explanation, so their local and global explanation is same.

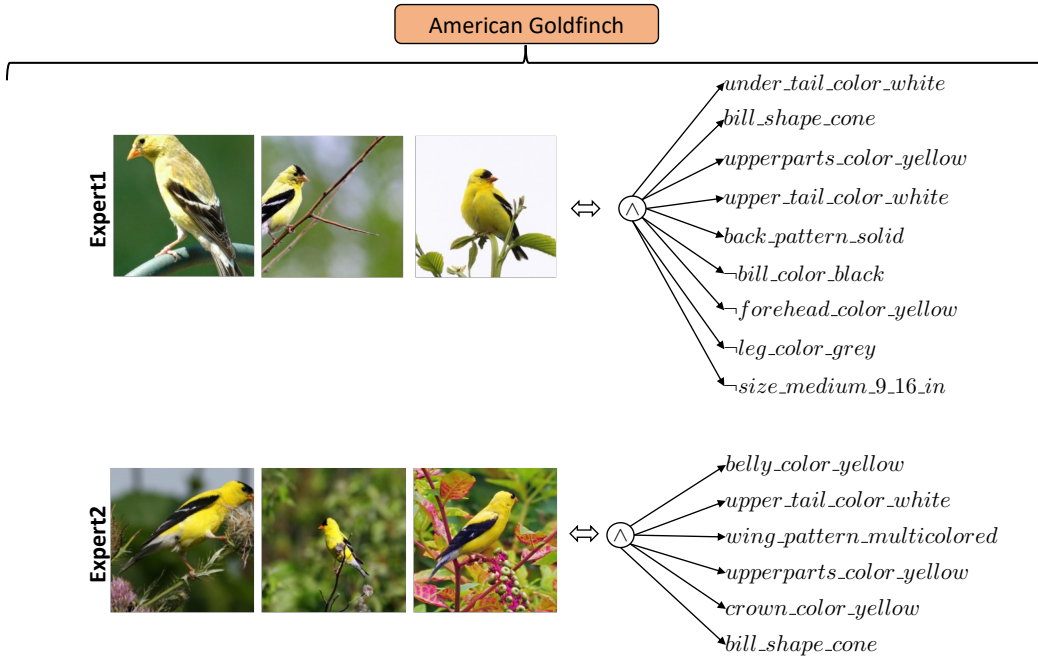


Figure 20: Generation of class-level explanations from VIT as a blackbox by combining the local explanations of “American Goldfinch” by expert1(top row) and expert2 (bottom row). Note that all the samples have same local explanation, so their local and global explanation is same.

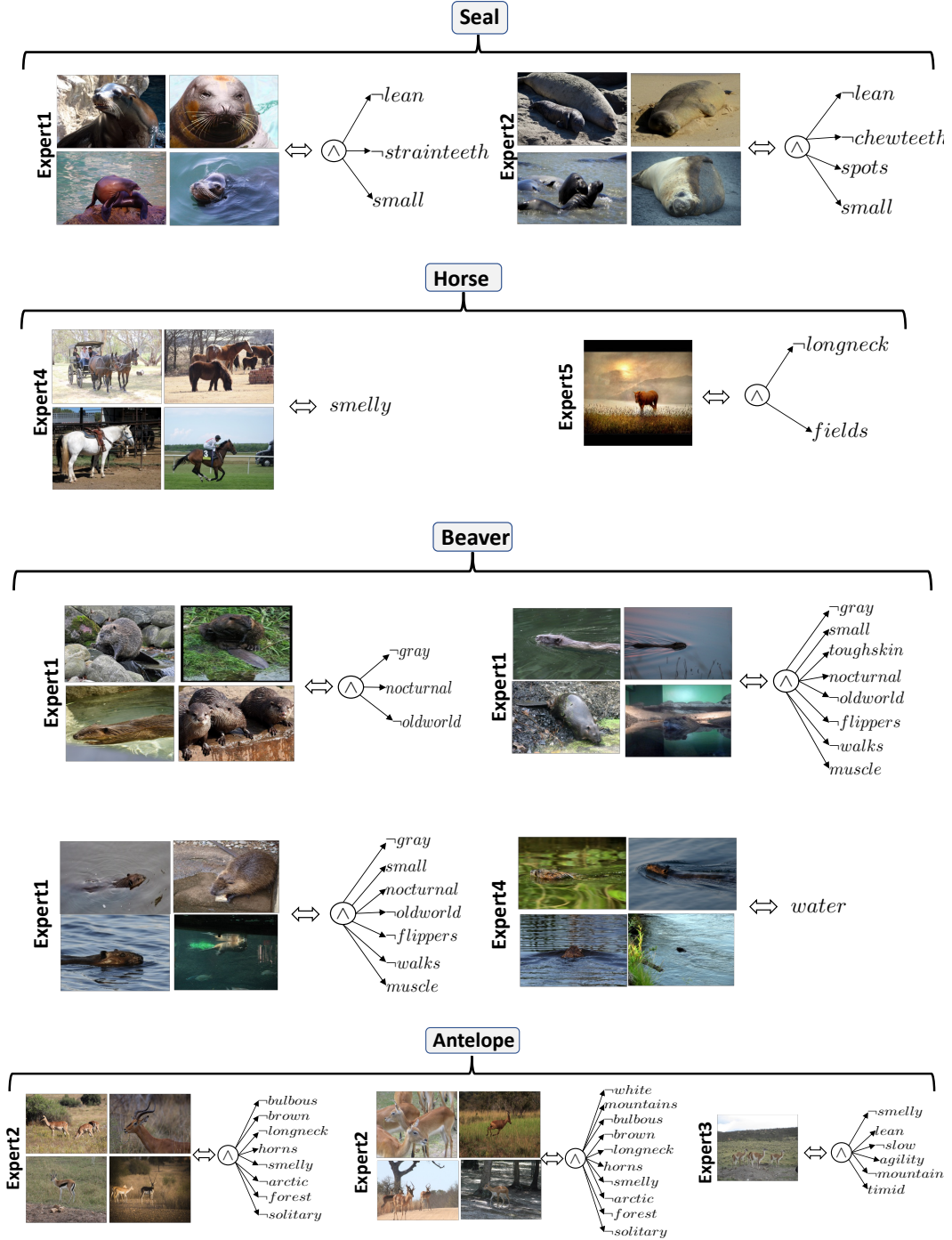


Figure 21: Examples of “Local explanations” by MoIE for Awa2 dataset. This figure captures the variability of explanations for different samples for identifying an animal species as “Seal”, “Horse” and “Beaver” respectively. Each FOL explains the set of images shown in the figure for an expert. For example to explain a Beaver (3rd row), expert4 utilizes the concept *water*. However, the expert1 explains the first set of images as “Beaver” due to of *graynocturnal* and *oldworld*. For the 2nd set of images, expert1 also employs the absence of other concepts such as *flippers*, *walks* etc.along with the previous concepts to classify “Beaver”. In total expert3 constructs three sets of FOLs, explaining a specific set of samples locally as per our hypothesis.

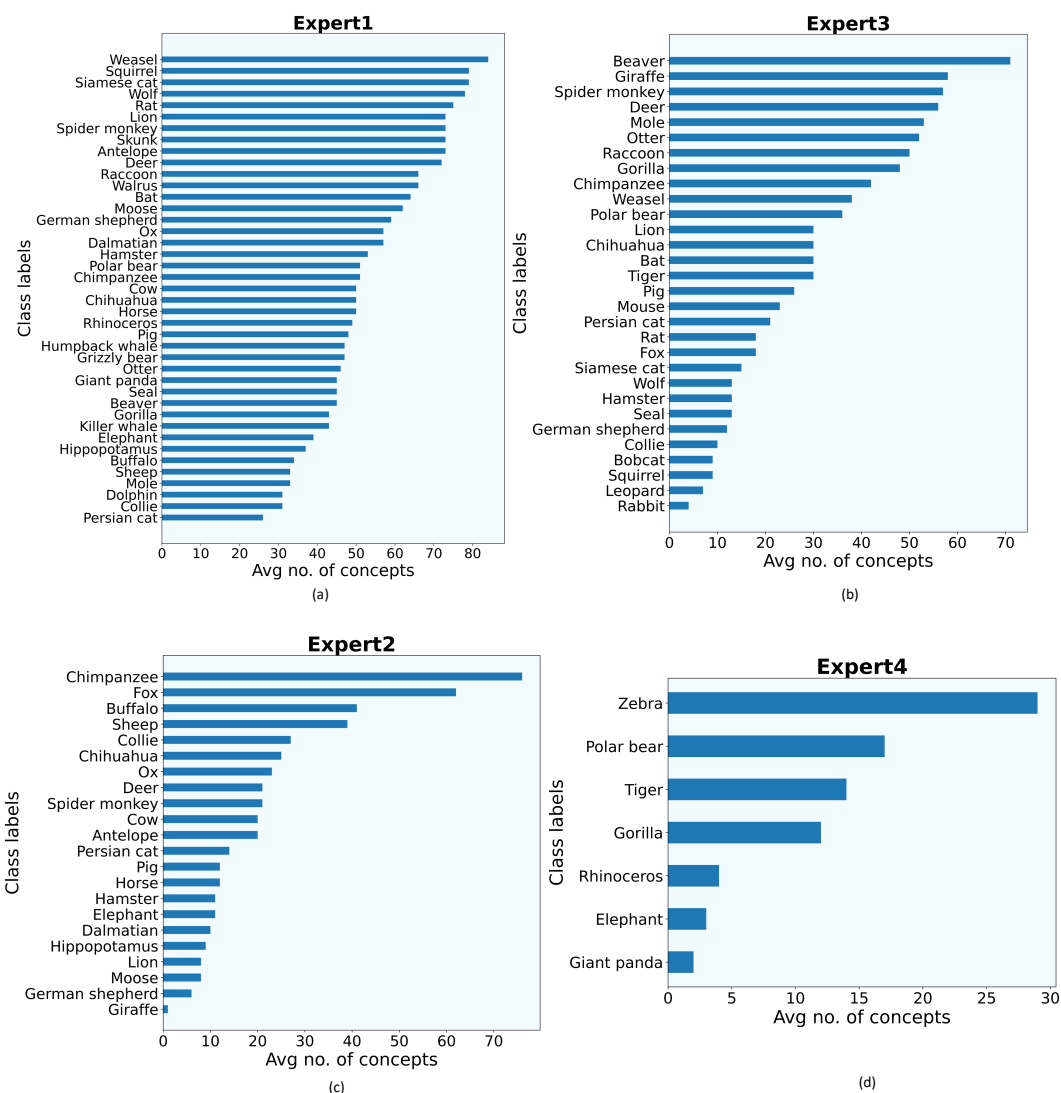


Figure 22: Class labels (Animal species) vs avg concepts using ResNet-101 as backbone for Awa2. Each bar in this plot indicates the average number concepts required to explain each sample of that animal species correctly. For example according to (a) expert1 requires approximately 80 concepts to explain an instance of “Weasel”.

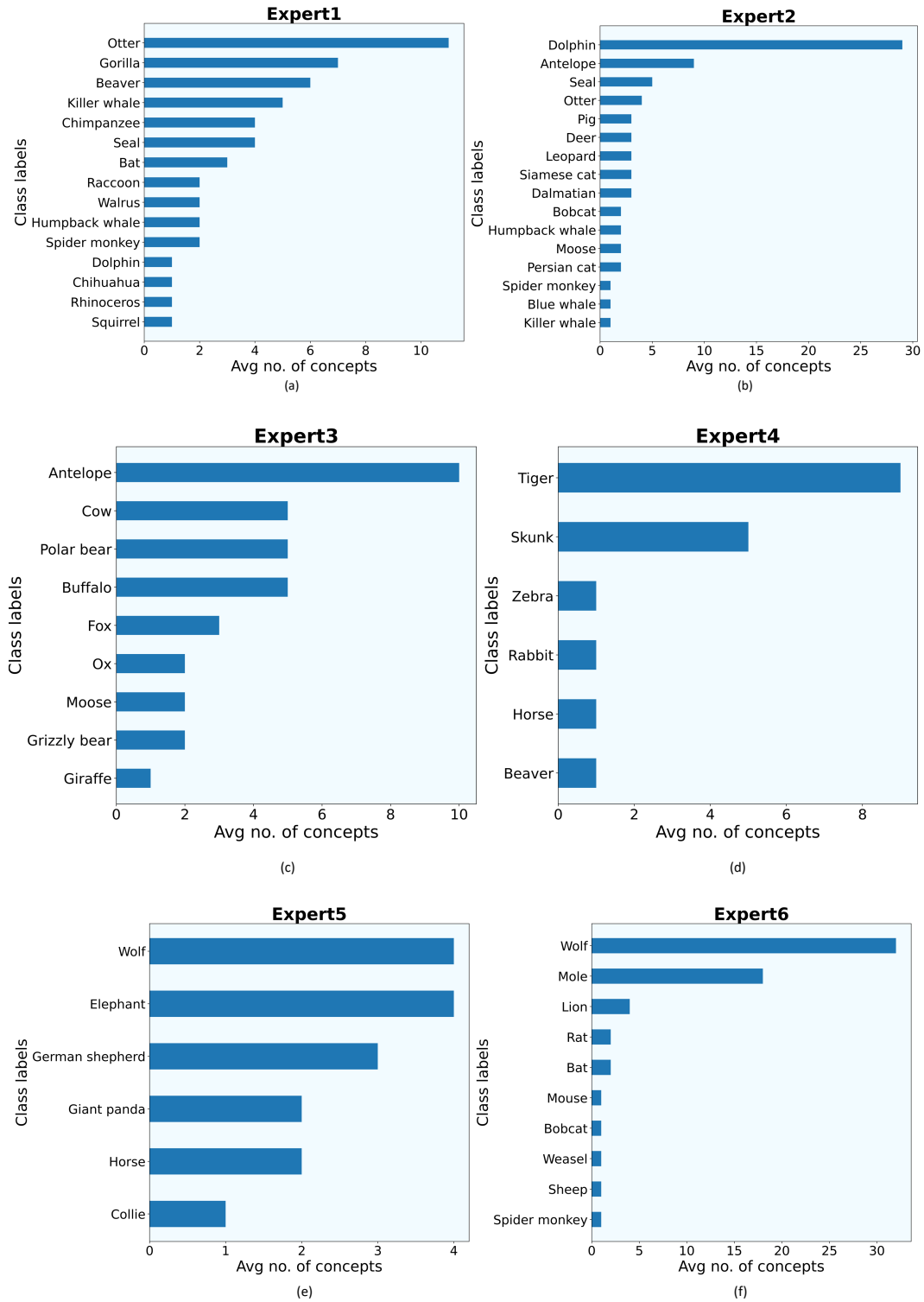


Figure 23: Class labels (Animal species) vs avg concepts using VIT as backbone for Awa2. Each bar in this plot indicates the average number concepts required to explain each sample of that animal species correctly. For example according to (a) expert1 requires approximately 80 concepts to explain an instance of “Otter”.

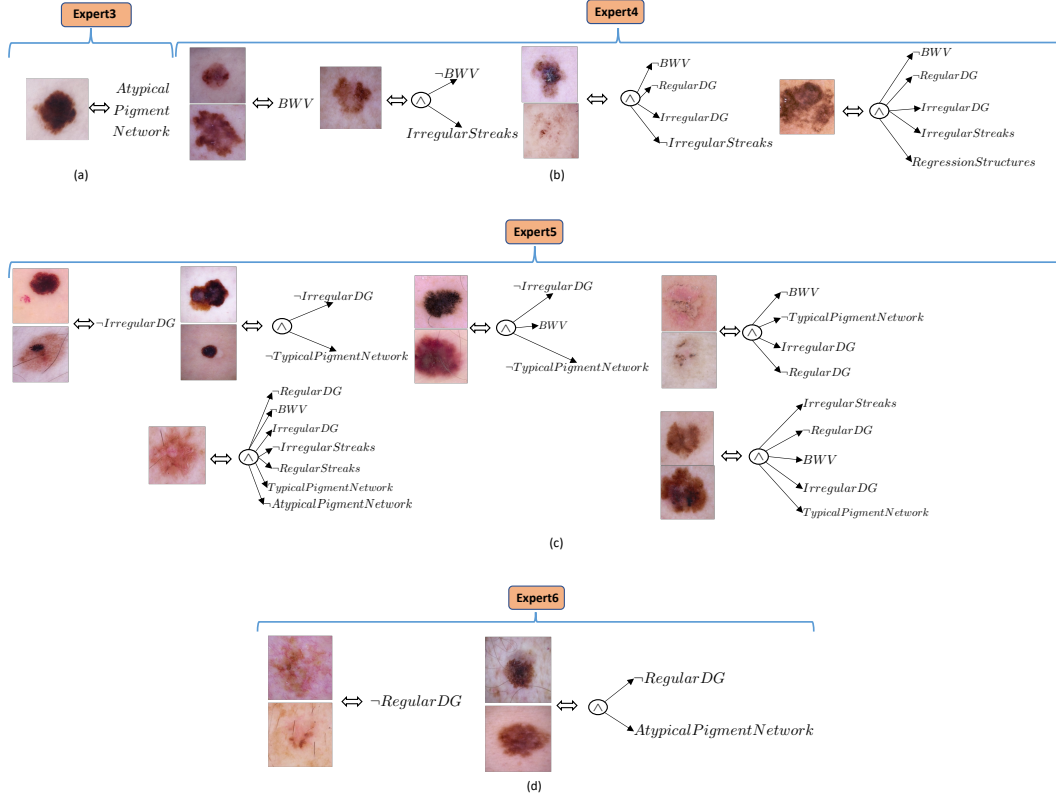


Figure 24: Examples of “Local explanations” by MoIE for identifying a skin lesion as “Malignant” in HAM10000 dataset. Each FOL explains the set of images shown in the figure for an expert. For example, in (a), expert3 identifies all the covered samples as “Malignant” due to the concept *Atypical Pigment Net*. However, in (b), the expert4 explains “Malignancy” using four sets of FOLs, explaining a specific set of samples locally as per our hypothesis. It uses *BWV* to classify “Malignancy” for the first set (left of b) of images. For the 2nd set of images, expert4 considers *BWV* and *Irregular Streaks* to classify a skin lesion as “Malignant”. Experts 5 and 6 constructs similar FOLs explaining a set of samples locally.

A.7.8 SAMPLE IMAGES COVERED BY EACH VIT-DERIVED EXPERT AND THE FINAL RESIDUAL OF CUB-200

Figure 29 compares different sample images covered by different VIT-derived experts and the final residuals of CUB-200. Figure 30 shows more instances, covered by the VIT-derived final residual of CUB-200. Table 6 compares the performance of the final residual with that of the blackbox (f^0). The second column of the table shows the performance of the blackbox (f^0) on the samples covered by the final residual. The third column shows the performance of the blackbox (f^0) on all the samples in the test set. Clearly, this table shows that the performance of the blackbox (f^0) drops substantially for the samples covered by the final residual. For example, for HAM10000, the overall performance of the blackbox (f^0) is 92.15%. However, on the samples covered by the final residual, the performance of the blackbox (f^0) drops to 67.89%. This experiment demonstrates that the final residual is left with relatively “harder” samples to explain.

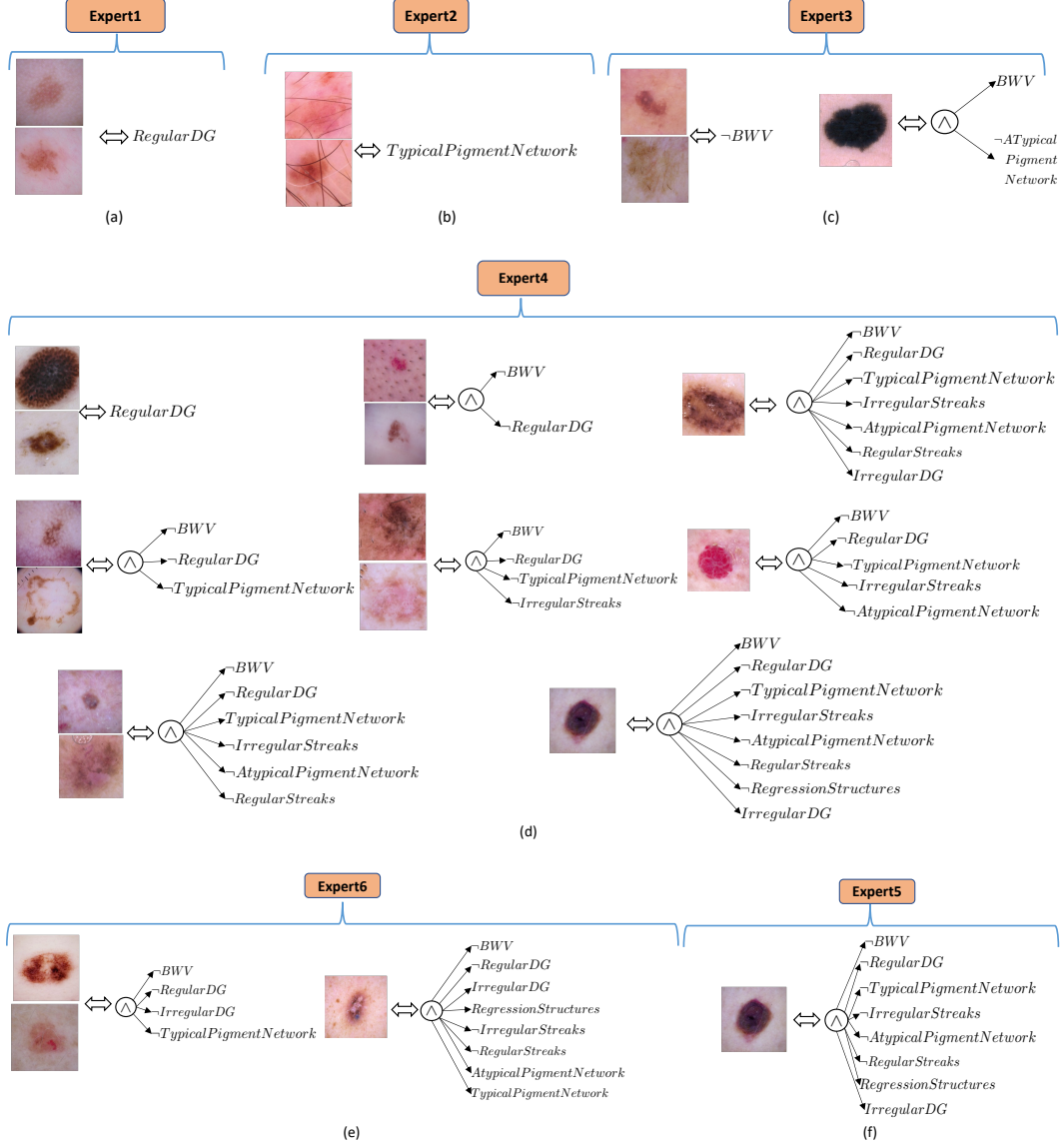


Figure 25: Examples of “Local explanations” by MoIE for identifying a skin lesion as “Benign” in the HAM10000 dataset. Each FOL explains the set of images shown in the figure for an expert. For example, in (a), expert1 identifies all the covered samples as “Benign” due to the concept *RegularDG*. However, in (c), the expert3 explains the first set (left of c) of images as “Benign” due to the absence of *BWV*. For the 2nd set of images (right of c), expert3 also considers the absence of *Atypical Pigment Net* along with *BWV* to classify “Benign”. Thus expert3 constructs two sets of FOLs, explaining a specific set of samples locally as per our hypothesis. Experts 4, 5 and 6 constructs similar FOLs explaining a set of samples locally.

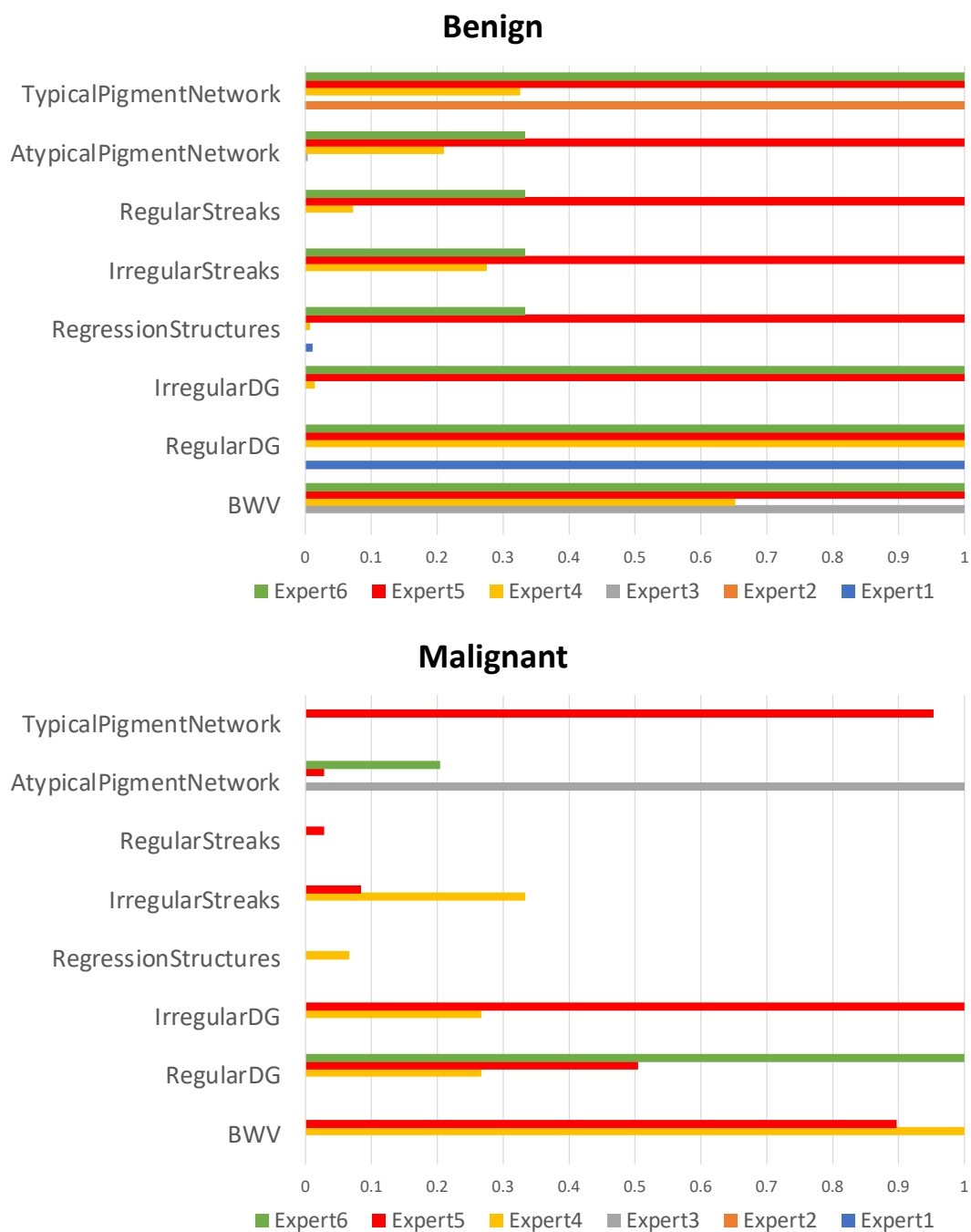


Figure 26: Concept frequency per expert. From top to down, for each expert, bar plot showing the importance of a concept for predicting a skin lesion as Benign and Malignant respectively. For example, *Atypical Pigment Network* concept plays a crucial role for predicting “Malignant” skin lesion by expert3 as is present in all the local explanations for expert5.

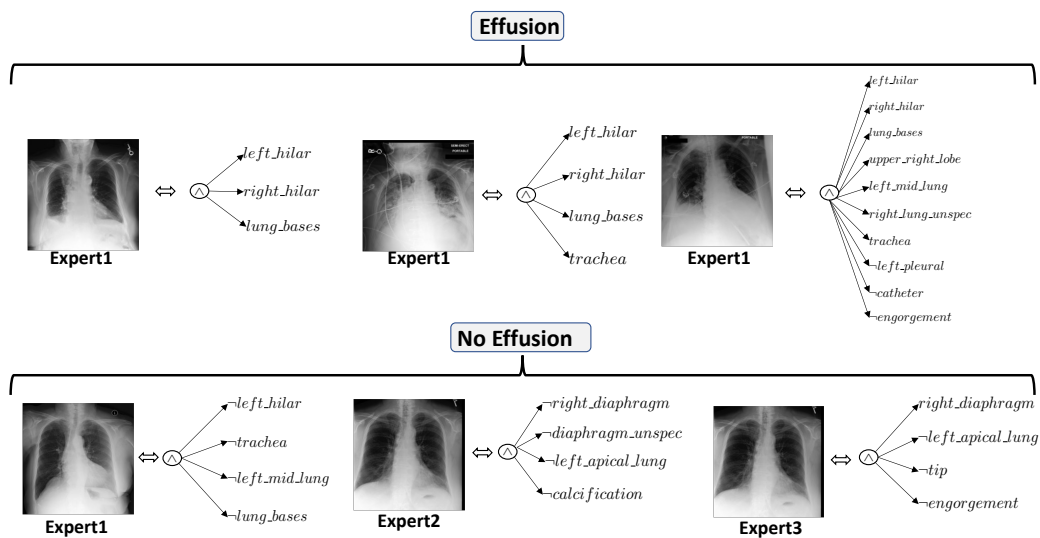


Figure 27: Examples of local explanation for “Effusion” and “No Effusion” in MIMIC-CXR dataset.

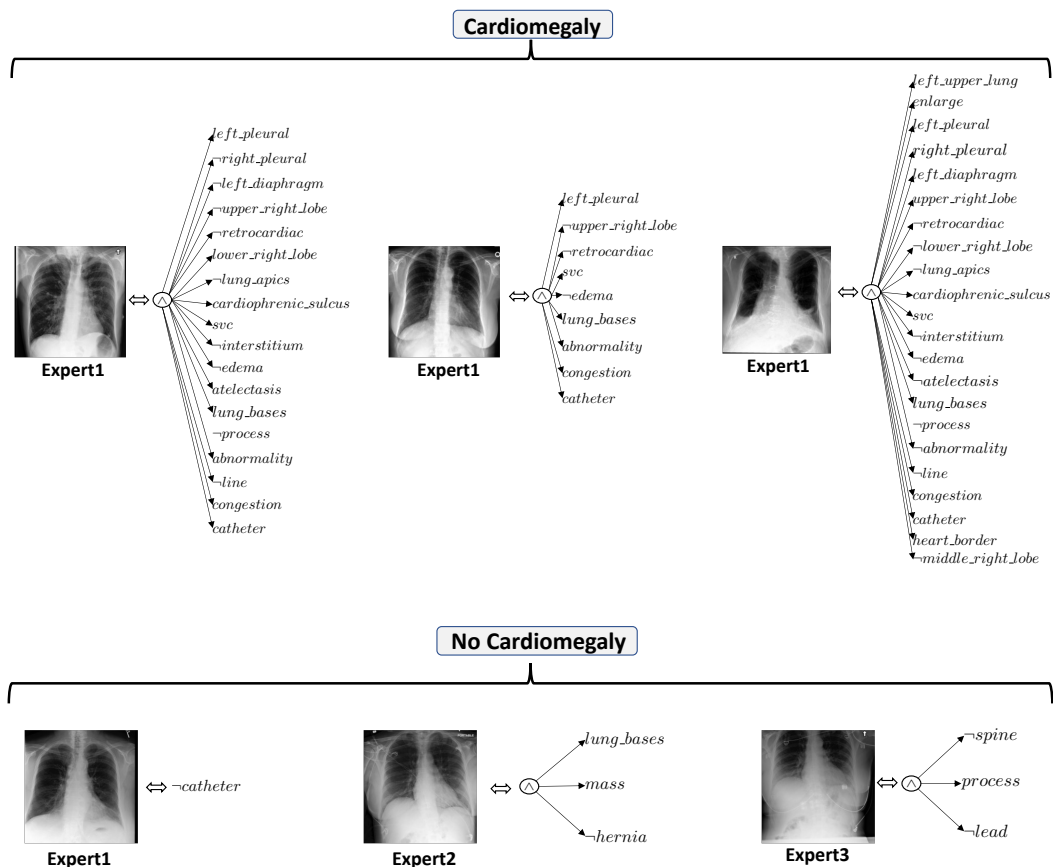


Figure 28: Examples of local explanation for “Cardiomegaly” and “No Cardiomegaly” in MIMIC-CXR dataset.

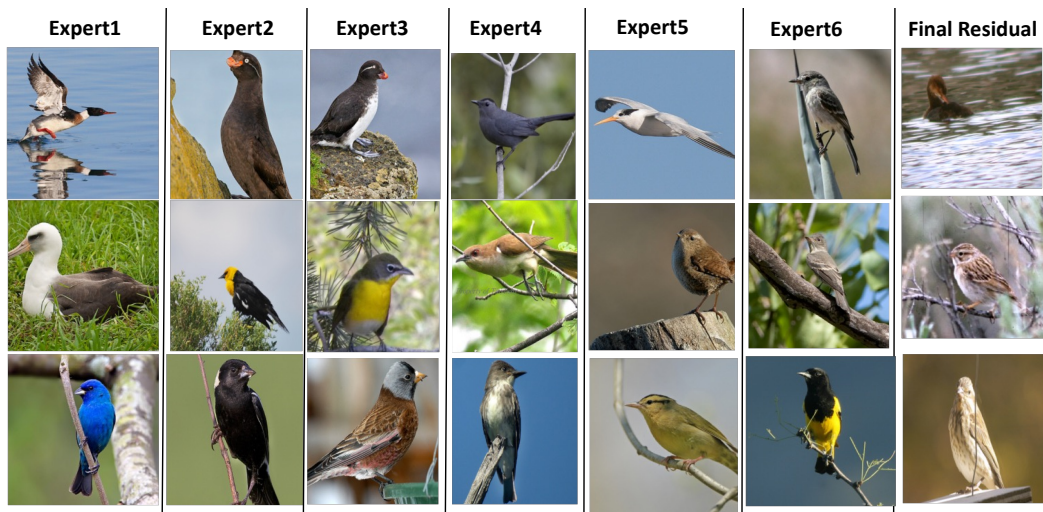


Figure 29: Sample images covered by each VIT-derived expert and the final residual of CUB-200.



Figure 30: More images covered by the VIT-derived final residual of CUB-200.

Table 6: Comparison of performance (Accuracy, %) of the final residual and the blackbox (f^0) on held-out test set. The 2nd column depicts the performance of the initial blackbox (f^0) on the samples of the test set. To compare fairly, we dispatch the samples, covered by the final residual through the blackbox (f^0) and compare the performance of the blackbox on these samples with the final residual (3rd column). We observe that the performance of blackbox on the samples covered by the final residual is lower than that of the blackbox on all the samples for all the dataset.

Dataset (Architecture)	On all samples	On selected samples covered by the final residual (residual, blackbox)
Cub-200 (ResNet-101)	88.64	(82.52, 85.41)
Cub-200 (ViT)	91.30	(81.01, 83.01)
Awa2 (ResNet-101)	91.02	(77.88, 79.11)
Awa2 (ViT)	98.53	(92.56, 93.56)
HAM10000 (Inception)	92.15	(67.89, 62.89)
Effusion from MIMIC-CXR (DenseNet-121)	78.34	(35.71, 37.06)
Cardiomegaly from MIMIC-CXR (DenseNet-121)	84.89	(48.71, 51.06)